Two-Dimensional Materials for Highly Efficient and Stable Perovskite Solar Cells

Xiangqian Shen[1,2], Xuesong Lin[1], Yong Peng[4], Yiqiang Zhang[5], Fei Long[6], Qifeng Han[1], Yanbo Wang[1] ✉, Liyuan Han[1,3] ✉

HIGHLIGHTS

- Recent progress on the applications of 2D materials in perovskite solar cells is discussed from the views of bottom interfaces, top interfaces, and electrodes.

- The roles of van der Waals heterojunction in enhancing the performance of perovskite solar cells are highlighted.

- The future directions and challenges in development of 2D materials-based perovskite solar cells are provided.

ABSTRACT Perovskite solar cells (PSCs) offer low costs and high power conversion efficiency. However, the lack of long-term stability, primarily stemming from the interfacial defects and the susceptible metal electrodes, hinders their practical application. In the past few years, two-dimensional (2D) materials (e.g., graphene and its derivatives, transitional metal dichalcogenides, MXenes, and black phosphorus) have been identified as a promising solution to solving these problems because of their dangling bond-free surfaces, layer-dependent electronic band structures, tunable functional groups, and inherent compactness. Here, recent progress of 2D material toward efficient and stable PSCs is summarized, including its role as both interface materials and electrodes. We discuss their beneficial effects on perovskite growth, energy level alignment, defect passivation, as well as blocking external stimulus. In particular, the unique properties of 2D materials to form van der Waals heterojunction at the bottom interface are emphasized. Finally, perspectives on the further development of PSCs using 2D materials are provided, such as designing high-quality van der Waals heterojunction, enhancing the uniformity and coverage of 2D nanosheets, and developing new 2D materials-based electrodes.
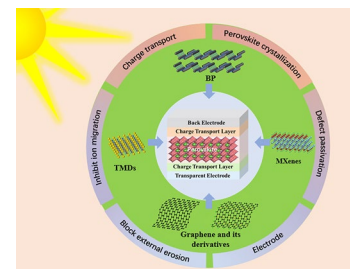
KEYWORDS Perovskite solar cells; Two-dimensional materials; Interface engineering; Van der Waals heterojunction; Electrodes

Xiangqian Shen and Xuesong Lin have contributed equally to this work.

✉ Yanbo Wang, sjtu-wyb@sjtu.edu.cn; Liyuan Han, han.liyuan@sjtu.edu.cn

1 State Key Laboratory of Metal Matrix Composites, Shanghai Jiao Tong University, Shanghai 200240, People's Republic of China
2 Xinjiang Key Laboratory of Solid State Physics and Devices, School of Physical Science and Technology, Xinjiang University, Urumqi 830046, People's Republic of China
3 Special Division of Environmental and Energy Science, College of Arts and Sciences, Komaba Organization for Educational Excellence, University of Tokyo, Tokyo 153-8902, Japan
4 State Key Laboratory of Advanced Technology for Materials Synthesis and Processing, Wuhan University of Technology, Wuhan 430070, People's Republic of China
5 College of Chemistry, Henan Institute of Advanced Technology, Zhengzhou University, Zhengzhou 450001, People's Republic of China
6 Guangxi Key Laboratory of Optical and Electronic Materials and Devices, Collaborative Innovation Center for Exploration of Nonferrous Metal Deposits and Efficient Utilization of Resources, School of Materials Science and Engineering, Guilin University of Technology, Guilin 541004, People's Republic of China

1 Introduction

In the past decade, perovskite solar cells (PSCs) have attracted a lot of attention due to their excellent optoelectronic properties, low cost, and facile manufacturing process [1–7]. Researchers have dedicated efforts to enhancing the power conversion efficiency (PCE) and stability of PSCs through various strategies such as architecture design [8, 9], composition engineering [5, 10], charge transport layer (CTL) optimization [11, 12], defect passivation [6, 13], and interface modification [14, 15]. Notably, the state-of-the-art PSCs achieved a certified PCE exceeding 26%, which is comparable to that of monocrystalline silicon solar cells [16–19]. However, there are still challenges that need to be overcome for commercialization, including the notorious interfaces and unsatisfactory electrodes. These issues hinder the progress of PCE in reaching the Shockley–Queisser limit and maintaining long-term stability under external environmental conditions [20–23].

In the case of a typical PSC, the interfaces are composed of electrodes, CTLs, and perovskite [24, 25]. Due to the incompatibility between materials in terms of crystal lattice, thermal expansion coefficient, energy level, and carrier mobility, these interfaces are characterized by a high defect state density and low ion migration barriers [21, 26, 27]. Furthermore, the solution-processed polycrystalline perovskite, along with its ionic nature, makes these issues even more severe [28–31]. Therefore, the carrier accumulation, non-radiative recombination, and degradation reactions usually occur at the interfaces of PSCs, which leads to a decrease in both device efficiency and stability [32–35]. In addition, the durability of PSCs is constrained by the traditional metal electrodes that are susceptible to the migrated ions from the perovskite [22, 36]. As for the flexible PSCs, the poor mechanical stability of the transparent conductive oxides is also a weakness [37, 38]. Therefore, there is an urgent need to improve the interface quality and develop new electrode materials to realize efficient and stable PSCs.

Two-dimensional (2D) materials are ultrathin materials that can be only a few atoms thick, providing unique properties that are different from their bulk counterparts [39, 40]. In the past few years, various 2D materials, including graphene and its derivatives, transitional metal dichalcogenides (TMDs), transitional metal carbides and/or nitrides (MXenes), and black phosphorus (BP) have been developed and demonstrated exceptional performance in fields such as transistors, sensors, biomedicine, catalysts, and photovoltaic cells [41–45]. The first application of 2D materials in PSCs can be traced back to 2013 when H.J. Snaith and colleagues enhanced the PCE of mesoporous PSCs from 10.0% to 15.6% by modifying the TiO_2 electron transport layer (ETL) using graphene nanoflakes [46]. This enhancement is attributed to the exceptional conductivity of graphene and its optimal work function (WF) situated between the conduction bands of FTO and TiO_2, which provide a highway for electron transportation and collection.

Soon thereafter, researchers recognized that 2D materials are desirable for use as the interface and electrode materials in PSCs, mainly due to the following advantages: firstly, 2D materials are notable for their atomic-level thickness, smooth surfaces, and lack of dangling bonds [54]. Unlike traditional interface contacts, 2D materials form van der Waals (vdW) heterostructures through physical adsorption with other materials, thereby minimizing the formation of defects at the interface [55]. This unique interaction has been shown to facilitate the epitaxial growth of perovskite thin films, optimizing their crystallization and orientation [51, 56]. Secondly, the electronic structure of 2D materials, including their band gap and WF, is significantly influenced by their atomic layers and surface functional groups. This offers the opportunity for precise manipulation of interface barriers, minimizing the energy loss during carrier extraction and transport across the interfaces [57, 58]. Thirdly, due to the superior conductivity, some of 2D materials can function as the electrode to realize efficient charge collection [59, 60]. Moreover, 2D materials possess excellent chemical and mechanical stability with high compactness, which render them resistant to moisture, oxygen, ion migration, and metal diffusion. Based on all these benefits, 2D materials successfully find their applications in perovskite crystallization, charge transport, defect passivation, and electrode (Fig. 1) [45, 61–63].

In this review, recent advancements in the incorporation of 2D materials into PSCs are summarized. To gain a deeper understanding of 2D materials and the interfaces they form, we first present a brief introduction to the fundamental properties of 2D materials and vdW heterostructures based on them. Then, we focus on the applications of 2D materials at the bottom interfaces, top interfaces, and electrodes of PSCs, respectively. We also delve into the underlying mechanisms

that contribute to improved device efficiency and stability. At the end of this review, the conclusions and possible pathways toward unlocking the full potential of 2D materials-incorporated PSCs are outlined.

2 2D Materials and Van der Waals Heterojunctions

2D materials are defined as nanoscale materials ranging from 1 to 100 nm, which derive into a wide range of electronic properties including conductors (metal and semi-metal), semiconductors (direct and indirect bandgap), and insulators [39, 56, 57]. The confinement of carrier mobility gives rise to a plethora of peculiar properties and applications, such as bandgap tunability for photoelectric devices, spin controllability for spintronics, and structure anisotropy for various polarized devices [54, 64, 65]. Furthermore, the integration of 2D materials with other functional layers is a vital approach for forming semiconductor heterojunctions or electric contacts, which can integrate diverse properties into modern optoelectronic devices. Notably, vdW heterojunctions can be physically assembled through weak vdW interactions, without limitations in regard to lattice matching and processing compatibility.

This significant advantage enables the extensive applications of 2D materials on the photovoltaics interfaces [55, 66]. In Sect. 2, we summarize the category of 2D materials and analyze their basic properties, as well as discuss the vdW heterojunctions of 2D materials.

2.1 Category and Basic Properties of 2D Materials

Currently, the four most commonly utilized 2D materials in PSCs are graphene and its derivatives, TMDs, MXenes, and BP [45, 57, 61]. Besides, other 2D materials such as antimonene, hexagonal boron nitride (h-BN), metal-free carbon nitrides (CNs), metal–organic frameworks (MOFs), and 2D perovskite materials have also been reported in PSCs [67–71]. The basic properties of typical examples are summarized in Table 1.

The graphene and its derivatives possess atomic layers arranged in a hexagonal honeycomb lattice. As the first investigated 2D material, graphene is an atomically thin sp^2 carbon layer arranged in a hexagonal honeycomb lattice [40]. As reported by previous works [72, 73], the mechanical stability of the 2D materials described as cohesive energy is inversely proportional to the bond length. Among the 2D materials, high-symmetry graphene shows the shortest
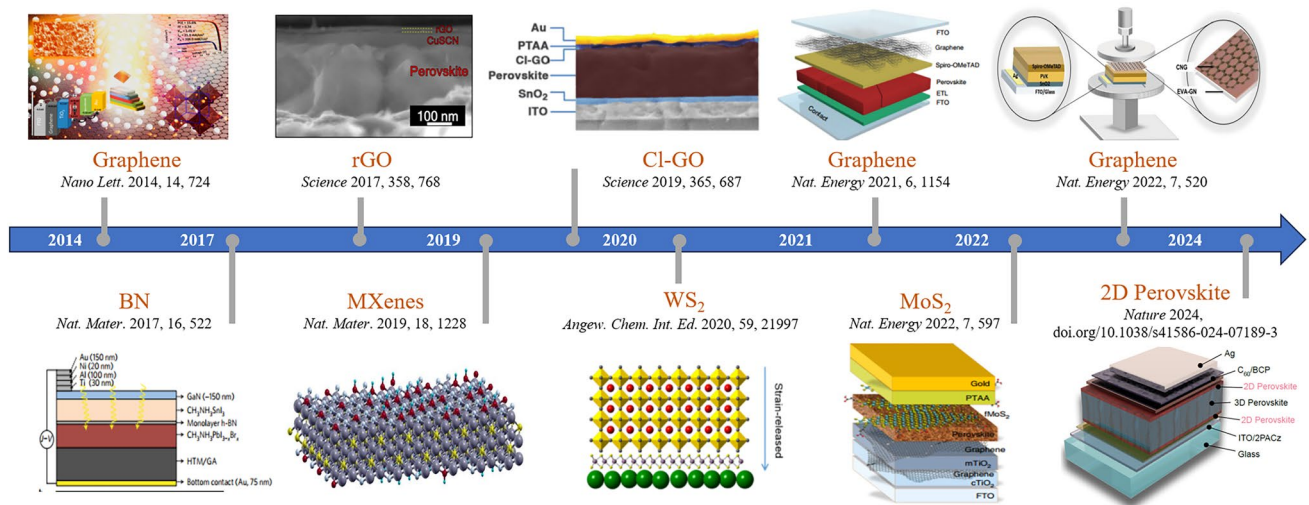

Fig. 1 The key milestones of 2D materials-incorporated PSCs over the past decade. Reproduced with permission from Ref. [46]. Copyright 2013, American Chemical Society. Reproduced with permission from Ref. [47]. Copyright 2016, Springer Nature. Reproduced with permission from Ref. [48]. Copyright 2017, AAAS. Reproduced with permission from Ref. [49]. Copyright 2019, Springer Nature. Reproduced with permission from Ref. [50]. Copyright 2019, AAAS. Reproduced with permission from Ref. [51]. Copyright 2020, Wiley. Reproduced with permission from Ref. [52]. Copyright 2021, Springer Nature. Reproduced with permission from Ref. [53]. Copyright 2022, Springer Nature. Reproduced with permission from Ref. [36]. Copyright 2022, Springer Nature. Reproduced with permission from Ref. [8]. Copyright 2024, Springer Nature

bond length, making it the most stable 2D material known to date. The electronic bands near the six corners of the 2D hexagonal Brillouin zone cross the Fermi level, resulting in a linear alteration of electron energy of a band within the Brillouin zone at these points. This unique feature gives rise to a zero effective mass for carriers and imparts graphene with semi-metal properties, ultimately endowing it with the highest recorded electron mobility up to 2×10^5 cm^2 V^{-1} s^{-1} at finite temperatures [39, 74]. The electronic structure engineering of graphene has rapidly progressed toward developing semiconducting modifications that exhibit an extremely low bandgap, thus paving the way for photovoltaics and electronic applications [39]. Nonetheless, these devices call for a requirement of larger bandgap semiconductors and insulators. Recently, researchers found that the properties of graphene and its derivatives, including the bandgap, conductivity, and dispersibility, can be precisely tuned through the regulation of functional groups and layer numbers [75, 76]. For example, the introduction of various groups to the graphene surface, such as epoxide, carbonyl, and hydroxyl groups, can yield GO [77]. The further chemical reduction process can transform GO into reduced GO (rGO). Unlike GO, which is an insulator, rGO displays a high conductivity while retaining the promising dispersibility of GO [78].

TMDs are a new star in the post-graphene era, which are composed of a transition metal and two chalcogens. The general stoichiometric formula of TMDs is MX$_2$, where M and X denoted the transition metal (Ti, V, Ta, Mo, W, Re, etc.) and chalcogen (S, Se, Te, etc.), respectively [89]. The structure of TMDs is layered with the transition metal sandwiched between two chalcogens, which are bound together by weak vdW forces that make it easy to be exfoliate into single or few layers. TMDs have a variety of electronic band structures, covering materials such as conductors, semimetals, semiconductors, insulators, and superconductors [84]. Some of the well-known and widely studied TMDs include molybdenum disulfide (MoS$_2$), tungsten disulfide (WS$_2$), tungsten diselenide (WSe$_2$), and molybdenum ditelluride (MoTe$_2$) [39, 90]. Recently, the layer-dependent characteristics of TMDs have attracted widespread attention. For example, when reducing from bulk to monolayer, MoS$_2$ undergoes a transition from an indirect bandgap to a direct bandgap, accompanied by an increase in bandgap energy from 1.2 eV to the range of 1.7–1.9 eV [44, 91]. In addition, monolayer MoS$_2$ exhibits photoluminescence and valley polarization in its electronic structure, which opens up possibilities for use in next-generation optoelectronic devices such as light-emitting diodes, lasers, and detectors [92].

MXenes are an emerging family of 2D materials that have attracted significant attention in materials science and nanotechnology due to their unique physical and chemical properties [42]. The general formula for MXenes is M$_{n+1}$X$_n$T$_x$ (n = 1–4), where M represents an early transition metal (Sc, Ti, Zr, Hf, V, Nb, Ta, Cr, Mo, etc.), X represents carbon and/or nitrogen, and T$_x$ stands for surface terminations such as –O, –OH, and –F [93]. MXenes have a layered structure similar to that of graphene but with a larger interlayer distance due to the presence of surface terminations. The monolayer or multilayer morphology of MXenes is typically synthesized from M$_{n+1}$AX$_n$ (MAX) phase precursors by removing the monoatomic layers of the A element, which belongs to group 13 or 14 (e.g., Al, Ga, Si, or Ge) [94]. MXenes possess a range of remarkable properties including high electrical conductivity, good mechanical strength, and excellent chemical stability [95]. In addition, the electronic structure and WF of MXenes can be facile tailored by modifying

Table 1 Basic properties of representative 2D materials

2D materials	Bandgap (eV)	Band type	Carrier mobility (cm^2 V^{-1} s^{-1})	Refs
Graphene	0	Direct	10^3 to 2×10^5	[79]
GO	2.00	Indirect	N/A	[80, 81]
rGO	0.02 to 2.00	Indirect to direct	1.2×10^2	[82]
h-BN	5.90	Direct	1	[83]
MoS$_2$	1.72	Direct	10 to 1.3×10^2	[44, 84]
Ti$_3$C$_2$T$_X$	1.05	Direct	3.4×10	[85]
Phosphorene	1.67	Direct	7×10^2 to 2.6×10^4	[86]
BP	1.60	Direct	10^4 to 2.6×10^4	[87]
Antimonene	1.75	Indirect	10^5 to 4×10^5	[88]

their surface terminations. Typical MXenes include Ti_2CT_x, $Ti_3C_2T_x$, Nb_2CT_x, and $(Mo, V)_5C_4T_x$. Notably, $Ti_3C_2T_x$ was first reported and is widely used in PSCs [96, 97].

BP is a layered material that consists of single or multiple layers of phosphorus atoms arranged in a honeycomb structure. It has a puckered structure resulting from the strong covalent bonds within each layer and weak vdW interactions between layers [98–100]. The intricate structure endows BP high in-plane anisotropy, meaning its electrical and optical properties vary depending on the orientation of the layer with respect to the crystalline axis. BP has a direct bandgap that can be adjusted by its thickness. One of the most exceptional features of BP is its high carrier mobility, which allows for fast charge transport [101]. Moreover, the carrier transport in BP is dominated by quantum tunneling effects, which can lead to ambipolar behavior and strong nonlinearity [102]. These attributes enable BP to simultaneously transport n-type and p-type carriers, opening up new opportunities for field-effect transistors, optoelectronics, and photovoltaic devices [99]. Furthermore, BP boasts excellent mechanical properties with high tensile strength and ductility, making it a promising material for flexible electronics and stretchable devices [43].

2.2 Van der Waals Heterojunctions of 2D Materials

Integrating disparate materials with pristine interfaces is an indispensable step toward creating functional devices through deliberate design, which has been a longstanding objective of the material science community [54]. Currently, two dominant methods for constructing heterojunction have emerged, relying on either strong intramolecular interactions (e.g., covalent bond and ionic bond) or weak intermolecular interactions (e.g., vdW interaction) (Fig. 2a). The vdW interaction strength is typically of the order of 0.1–10 kJ mol^{-1}, about 2–3 orders of magnitude smaller than that of ionic or covalent bonds (about 100–1,000 kJ mol^{-1}) [55].

Although chemical bonds yield strong interfacial bonding, the success of this strategy depends on highly matched lattices and one-to-one paired bonding atoms between the surfaces of materials. Materials with lattice mismatch of greater than 5% result in a lot of dangling bonds and severe interface disorder, which could degrade intrinsic properties of the corresponding devices (Fig. 2b, c) [39, 103]. On the contrary, vdW heterojunctions are integrated via the physical assemble of pre-fabricated building blocks through weak vdW forces, thus presenting an alternative approach to low-energy material integration. This physical assembly does not rely on the direct chemical bonding and bypasses the constraints of lattice matching and compatibility of synthesis conditions
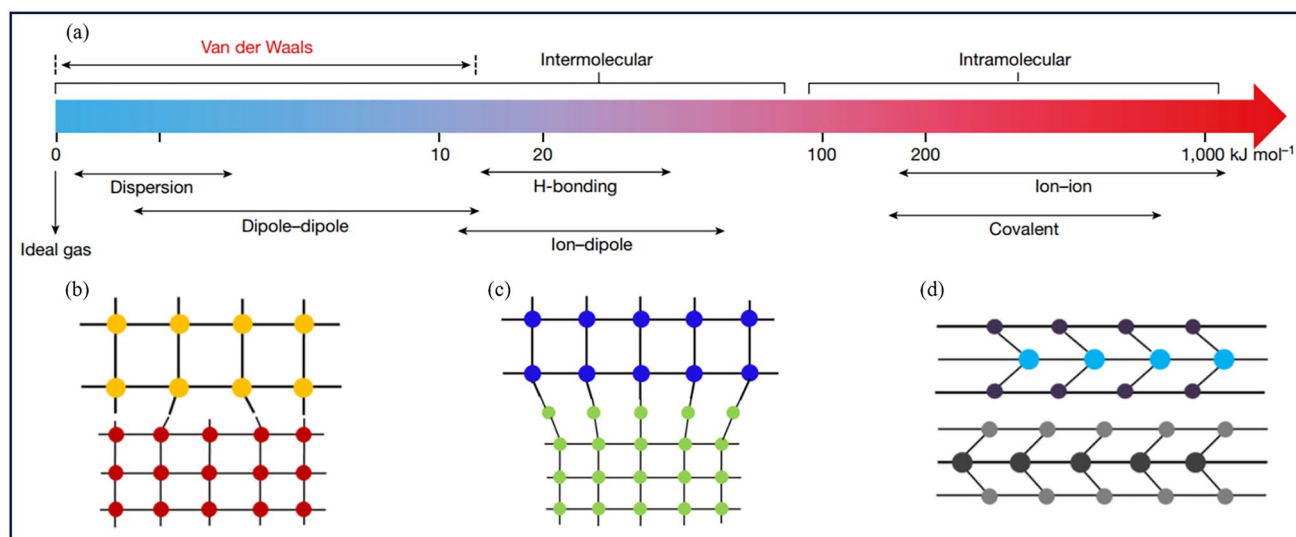

Fig. 2 a Energies of various molecular interactions. The vdW interaction is the weakest intermolecular interaction (also termed physical interaction), much smaller than typical intramolecular interactions (also termed chemical interactions). Reproduced with permission from Ref. [55]. Copyright 2019, Springer Nature. **b-d** Schematic illustration of the interfaces connected by **b** covalent bonds, **c** ionic bonds, and **d** vdW interaction. Reproduced with permission from Ref. [39]. Copyright 2013, American Chemical Society

(Fig. 2d) [104]. Therefore, this bond-free integration method exhibits no obvious restriction on material similarities and can be generally applied to construct feasible vdW heterojunctions between disparate materials with distinct crystal structures (e.g., crystallinity, lattice symmetry and constant), electronic properties (e.g., insulators, semiconductors, metals and superconductors), or material dimensions (e.g., 0D quantum dot, 1D nanowire, 2D nanosheet, and 3D bulk phase) [105–108]. The isolation of graphene and various 2D atomic materials with surfaces free of dangling bonds has sparked significant interest in vdW integration, which enables the creation of an array of heterojunctions with atomically clean and electronically sharp interfaces. This not only provides a fertile ground for fundamental studies, but also paves the way for exciting new device concepts [109].

In PSCs, the vdW heterostructure is created by combining of 2D materials with perovskite layers, with examples including graphene [110], MoS_2 [111], WS_2 [51], SnS_2 [112], WSe_2 [58], antimonene [113], and 2D perovskite [71]. These 2D materials typically function as templates, upon which the perovskite is epitaxially grown. This approach leads to the formation of a high-quality perovskite film with the following mechanism: (i) The 2D interlayer effectively serves as a physical barrier, which screens the defects and chemical interaction between the substrate and the perovskite film. (ii) The smoother 2D materials reduce surface roughness, enabling a longer atomic diffusion length and ultimately promoting the formation of larger crystalline grains. (iii) The low interfacial energy between 2D materials and perovskites prevents perovskite deformations during its growth process, which reduces the occurrence of voids and cracks within the thin films. Additional, these heterojunctions also enable effective photogenerated carrier transport and extraction through type II or quasi-type II junction [114]. By surface functionalizing 2D materials in these heterojunctions, charged defects (e.g., under-coordinated Pb cations, free I anions, interstitials, and substitution) can be passivated at both top and bottom perovskite interfaces, consequently reducing non-radiative recombination [115, 116]. Furthermore, vdW heterojunctions provide an excellent strategy to prevent ion migration in perovskite photovoltaics; for example, a 2D/3D vdW heterojunction based on graphene possesses a lattice parameter of 0.246 nm, which is smaller than the radius of I anions (0.412 nm), and thus precludes the corrosion of functional layers induced by ion migration [117]. In conclusion, the aforementioned

advantages of vdW heterojunctions hold great potential for interface modification and can enhance the efficiency and stability of ideal perovskite photovoltaics.

3 2D Materials at Bottom Interfaces

The bottom interface refers to the interface between the transparent electrode and the perovskite layer. For a regular device, the bottom interface includes the interfaces of transparent electrode/ETL and ETL/perovskite. Therefore, the main function of the bottom interface is to extract electrons from the active layer and conduct them to the transparent electrode [20]. On the other hand, the bottom interfaces of inverted device have an opposite configuration and direction of charge transport. The bottom interface, being the site for nucleation and growth of perovskite, plays a pivotal role in the formation of perovskite thin films. The crystal lattice constant, thermal expansion coefficient, and wettability of the bottom interface material directly influence the quality of the perovskite thin films, including their crystallinity, surface morphology, and optoelectronic properties [111, 118]. Moreover, since sunlight traverses the PSCs from the bottom to the top, the carrier concentration within the perovskite layer proximal to the bottom interface is higher than those present in other regions. Consequently, the bottom interface material must exhibit high carrier mobility and conductivity, alongside energy levels that are compatible with the perovskite film to prevent carrier aggregation and recombination [25, 31]. Besides, to guarantee optimal absorption and irradiation stability of the perovskite layer, it is required that the bottom interface has a high transmittance within the visible light spectrum while effectively shielding ultraviolet light [119–121]. In Sect. 3, we summarize the applications of 2D materials in enhancing the bottom interface of PSCs. The discussion focuses on their crucial role in enhancing the crystallization of perovskites, optimizing charge dynamics, and fine-tuning optical properties. Representative 2D materials at bottom interface for the enhancement of device efficiency and stability are illustrated in Table 2.

3.1 Graphene and Its Derivatives

Graphene was the earliest discovered and utilized 2D material in PSCs [46]. Due to its high conductivity and carrier

mobility, the interface modification by graphene can greatly improve the electrical contact between CTLs and perovskite films [59, 74]. Moreover, the inert and atomically smooth surface of graphene renders it an ideal template for the growth of perovskite materials. For instance, the vdW epitaxial growth of $CsPbBr_3$ thin films on a TiO_2 substrate can be achieved by overlaying a low-defect, large-area monolayer of graphene. This approach enables the formation of a high-quality $CsPbBr_3$ film, with an average grain size increased from 0.76 to 1.22 μm and improved (100) orientation [110]. However, the lack of a bandgap in graphene restricts its semiconductor applications. As derivatives of graphene, GO and rGO possess enhanced optoelectronic properties and solvent dispersibility, making them popular choices for applications in PSCs [77]. For example, to address the issue of photostability in poly[bis(4-phenyl)(2,4,6-trimethylphenyl)amine] (PTAA)-based inverted PSCs, a composite hole transport layer (HTL) combining rGO and PTAA has been proposed (Fig. 3a) [78]. When compared to pristine PTAA, the rGO/PTAA exhibits a superior absorptivity in the short-wave bands, thereby impeding the penetration of ultraviolet (UV) light into the perovskite layer (Fig. 3b). Moreover, rGO boasts a valence band maximum (VBM) of -4.97 eV, which forms a graded energy level between PTAA (-5.22 eV) and ITO (-4.7 eV). This strategy enables the PSC to achieve a satisfying PCE of 17.2% (active area of 1.02 cm^2), with an improved short-circuit current density (J_{SC}) and fill factor (FF) from 19.4 mA cm^{-2} and 69.9% to 20.3 mA cm^{-2} and 77.7%, respectively. Furthermore, the bilayer constructed PSCs exhibit outstanding light-soaking stability, maintaining ~ 90% of its original PCE after continuous illumination for 500 h at 100 mW cm^{-2}. As for the regular PSCs, SnO_2 ETL has been established for improving PCE and stability [131]. However, the semiconductor characteristics of this material strongly rely upon its inherent oxygen vacancies. It is important to maintain appropriate balance in the oxidation state of Sn, as SnO and SnO_2 exhibit p-type and n-type properties, respectively [132]. By incorporating a modest quantity of nitrogen-doped GO (NGO) as an oxidizing agent into the precursor solution of SnO_2, the oxygen vacancies are partially passivated and a conspicuous decrement in Sn^{2+} and increment in Sn^{4+} can be observed (Fig. 3d, e) [133]. Due to the enhancement in charge extraction and the reduction of non-radiative recombination, the open-circuit voltage (V_{OC}) of the device incorporating the SnO_2: NGO composite

layer is 60 meV higher than that of the device with pristine SnO_2.

By virtue of the intriguing quantum confinement effects, graphene quantum dots (GQDs) exhibit size-dependent bandgaps and remarkable surface-to-volume ratios [135]. These distinguishing features set them apart from conventional 2D graphene and broaden their functionalities at the bottom interface of PSCs. For example, the introduction of small amounts of GQDs with diameters ranging from 5–10 nm into an ethanol solution of $SnCl_2 \cdot 2H_2O$ yields a refined ETL of SnO_2: GQDs [134]. The optical bandgap of GQDs with such dimensions is ~ 2.4 eV, which is considerably narrower in comparison to that of SnO_2. In addition, the conduction band minimum (CBM) of GQDs is higher than that of SnO_2. Therefore, the photo-induced electrons in GQDs spontaneously transfer to the conduction band of SnO_2, subsequently filling the electron trap-state defects of SnO_2 (Fig. 3c). As a result, the electron trap-state density and WF of SnO_2:GQDs decline from an initial value of 4.30×10^{16} cm^{-3} and 4.35 eV to 1.23×10^{16} cm^{-3} and 4.01 eV, respectively. This modification improved the PCE of the device from the original 17.91% (with $V_{OC} = 1.101$ V, $J_{SC} = 22.10$ mA cm^{-2}, FF = 73.6%) to 20.31% (with $V_{OC} = 1.134$ V, $J_{SC} = 23.05$ mA cm^{-2}, FF = 77.8%).

In order to further improve the electronic structure and surface properties of GQDs, hetero-element doping and surface functionalization are important approaches [59]. To compare the effects of different doping elements on GQDs, the researchers synthesized three types of quantum dots: pristine GQDs, N-doped GQDs (NGQDs), and N and Cl co-doped GQDs (N,Cl-GQDs) [124]. Subsequently, these quantum dots are used to modulate the interface between (3,4-ethylenedioxythiophene):poly(styrenesulfonate) (PEDOT:PSS) HTL and Sn–Pb mixed perovskite. It has been found that the doping of N and Cl reinforces the p-type characteristics of GQDs and passivates the under-coordinated Sn/Pb cations in Sn–Pb mixed perovskite (Fig. 3f, g). Besides, the π-conjugated effect of the graphene structure and the electronegativity of Cl regulate the charge distribution at the interface, thereby facilitating hole extraction and conduction. The optimized PCE achieved for the three different types of PSCs were 18.6% for GQDs, 20.2% for NGQDs, and a remarkable 21.5% for N,Cl-GQDs. Significantly, the N,Cl-GQDs PSC demonstrated outstanding V_{OC} and FF values of 0.886 V and 80.4%, respectively, which are recognized as among the highest reported for Sn–Pb mixed PSCs.

Table 2 Representative 2D materials at the bottom interface for improving the efficiency and stability of PSCs

2D materials	Device structure	Function	PCE (%)	Characteristic and stability	Refs
Graphene	FTO/TiO$_2$/Graphene/CsPbBr$_3$/Carbon	vdW epitaxial growth of CsPbBr$_3$, improve the electron extraction	10.64	All-inorganic, HTL-free, 91% its initial PCE after 2,000 h in ambient air	[110]
rGO	ITO/rGO/PTAA/MAPbI$_3$/PCBM/BCP/Ag	Block ultraviolet light, gradient energy level between PTAA and ITO	17.2	Active area of 1.02 cm^2, 90% of its initial PCE after 1-sun illumination for 500 h	[78]
I-GQDs	ITO/SnO$_2$/I-GQDs/FAPbI$_3$/spiro-OMeTAD/Ag	Enhance the conductivity and eliminate surface defects of ETL, improve the crystallization of FAPbI$_3$	22.37	Over 84% of its initial PCE after 1-sun illumination for 500 h in a nitrogen gas glove box, without encapsulation, at room temperature	[122]
I-GQDs	ITO/SnO$_2$/I-GQDs/CsFAMA/spiro-OMeTAD/Ag	Passivate the defects of SnO$_2$, enhance UV light utilization through down-conversion	24.11	81% of its initial PCE after continuous UV irradiation (365 nm, 20 mW cm^{-2}) for 300 h	[123]
N,Cl-GQDs	ITO/PEDOT:PSS/N,Cl-GQDs /FAMA(Sn$_{0.6}$Pb$_{0.4}$)I$_3$/PCBM/BCP/Ag	Regulate the charge distribution and passivate the defect states	21.5	90% of its initial PCE after stored in glove box for 1,000 h without encapsulation	[124]
MoS$_2$	ITO/PTAA/MoS$_2$/MAPbI$_3$/PCBM/BCP/Ag	vdW epitaxy growth of MAPbI$_3$	20.55	80% of its initial PCE after 800 h in the dark ambient with 30% RH, without encapsulation	[111]
WS$_2$	FTO/SnO$_2$-TiO$_x$Cl$_{4-2x}$/WS$_2$/CsPbBr$_3$/Carbon	WS$_2$/CsPbBr$_3$ vdW heterostructure, release interfacial strain	10.65	All-inorganic, HTL-free. 90% of its initial PCE after continuous illumination for 10,000 s at 100 mW cm^{-2}; over 80% of its initial PCE after 120 days in ambient condition with 80% RH at 25 °C	[51]
WSe$_2$	ITO/NiO$_x$/WSe$_2$/FASnI$_3$/PCBM/BCP/Ag	vdW epitaxial growth, cascade band structure	10.47	Lead-free, 82% its initial PCE after 1,000 h in air condition with 20% RH, without encapsulation	[58]
SnS$_2$	FTO/SnO$_2$:SnS$_2$/CsPbBr$_3$/Carbon	Plays a role of "bridge" to connect incompatible interface, epitaxial growth	10.72	All-inorganic, HTL-free, 91% its initial PCE after 700 h in air condition with 80% RH and at 25 °C, without encapsulation	[112]
Ti$_3$C$_2$T$_x$	ITO/SnO$_2$-Ti$_3$C$_2$T$_x$/CsFAMA/spiro-OMeTAD/Au	Improve the dispersion and electronic property of the SnO$_2$ nanoparticles, induces a vertical growth of perovskite	23.07	90% its initial PCE after 500 h in ambient air with 30%~40% RH	[125]
Ti$_3$C$_2$T$_x$	PEN/ITO/Ti$_3$C$_2$T$_x$-PEDOT:PSS/CsFAMA/PCBM/BCP/Ag	Energy level alignment, facilitate charge extraction, improve the quality of perovskite film	17.06	Flexible, minimodule (15 cm^2), 90% its initial PCE after 1,200 h in ambient air at 85 °C	[126]
Ti$_3$C$_2$Cl$_x$	ITO/SnO$_2$-Ti$_3$C$_2$Cl$_x$/FAMAPb(I$_{0.95}$Br$_{0.05}$)$_3$/o-TB-GDY/spiro-OMeTAD/Au	Improve the perovskite crystallization, suppress non-radiative recombination by forming the Pb-Cl bond	24.86	92% its initial PCE after 1,464 h in ambient air; 80% its initial PCE after 1,002 h of thermal stability test at 85 °C	[127]
Nb$_2$CT$_x$	ITO/Nb$_2$CT$_x$/FA$_{0.85}$Cs$_{0.15}$PbI$_3$/spiro-OMeTAD/Ag	High conductivity, retards the crystallization process of perovskite	21.79	93% its initial PCE after 1,500 h in glovebox	[128]
BP	FTO/c-TiO$_2$/mp-TiO$_2$/BP-3/CsMAFAPb(I$_{0.83}$Br$_{0.17}$)$_3$/BP-1/spiro-OMeTAD/Au	Enhance charge extraction and light absorption, suppress carrier recombination	19.83	95% its initial PCE after 180 days in air, encapsulated with a parylene film	[129]
PNRs	ITO/PTAA:PNRs/MAPbI$_3$/PCBM/BCP/Cu	Enhance hole extraction, improve both the mobility and conductivity of the PTAA	21.14	N/A	[130]

Table 2 (continued)

2D materials	Device structure	Function	PCE (%)	Characteristic and stability	Refs
Antimonene	ITO/PTAA/Antimonene/MAPbI$_3$/PCBM/Bphen/Al	Enhance hole extraction and transport	20.11	N/A	[67]

Moreover, the introduction of imidazole bromide functionalized GQDs (I-GQDs) at the SnO$_2$/CH$_4$N$_2$HPbI$_3$ (FAPbI$_3$) interface elevates the carrier mobility of SnO$_2$ by a factor of 1.7 and improves the crystal quality of FAPbI$_3$. As a result, the PCE of the I-GQDs PSCs increased from 19.57% (with V_{OC} = 1.031 V, J_{SC} = 24.34 mA cm^{-2}, FF = 78%) to 22.37% (with V_{OC} = 1.073 V, J_{SC} = 25.42 mA cm^{-2}, FF = 82%) [122]. In recent progress, the down-conversion characteristics of I-GQDs have been demonstrated. By converting photons in the UV band into long-wavelength photons that can be absorbed, the PSCs incorporating I-GQDs achieved an impressive PCE of 24.11% (Fig. 3h) [123]. After continuous UV irradiation (365 nm, 20 mW cm^{-2}) for 300 h, ~81% of the initial PCE is retained.

3.2 Transitional Metal Dichalcogenides

As a highly promising 2D material, MoS$_2$ displays exceptional carrier mobilities and possesses an energy band structure that is ideally suited for a diverse range of optoelectronic applications [44, 89]. The VBM of the MoS$_2$ thin film is approximately -5.41 eV, which closely aligns with that of CH$_3$NH$_3$PbI$_3$ (MAPbI$_3$, -5.43 eV) [136]. The energy level alignment indicates MoS$_2$ flakes is a promising candidate of interlayers in MAPbI$_3$-based PSCs. For example, by adding a layer of MoS$_2$ between PTAA and MAPbI$_3$, the aging pathways at the interface were effectively suppressed. This approach is advantageous for the preparation of large-area PSCs. For a device with an active area of 0.5 cm^2, its PCE has been increased from 10.64% (control) to 13.17% (with MoS$_2$), with an improved V_{OC} from 0.949 to 1.009 V [137]. Furthermore, the MoS$_2$-based PSCs achieved a T_{80} lifetime of 568 h, which represent the state-of-the-art for PSCs at that time. Due to its smooth and dangling bond-free surface, MoS$_2$ also serves as an epitaxial growth template for MAPbI$_3$ and form a vdW heterojunction between them. In detail, the MAPbI$_3$ (008) and MoS$_2$ (110) planes have an identical interplanar distances of 1.58 Å, which promotes the out-of-plane growth of perovskite films with a preferred crystal orientation along the (110) axis (Fig. 4a-c) [111]. As a result, the average grain size of MAPbI$_3$ increased from 290 to 526 nm, accompanied by a decrease in defect state density from 2.59×10^{16} to 1.17×10^{16} cm^{-3}. Through the modification of MoS$_2$, the PCE of the inverted
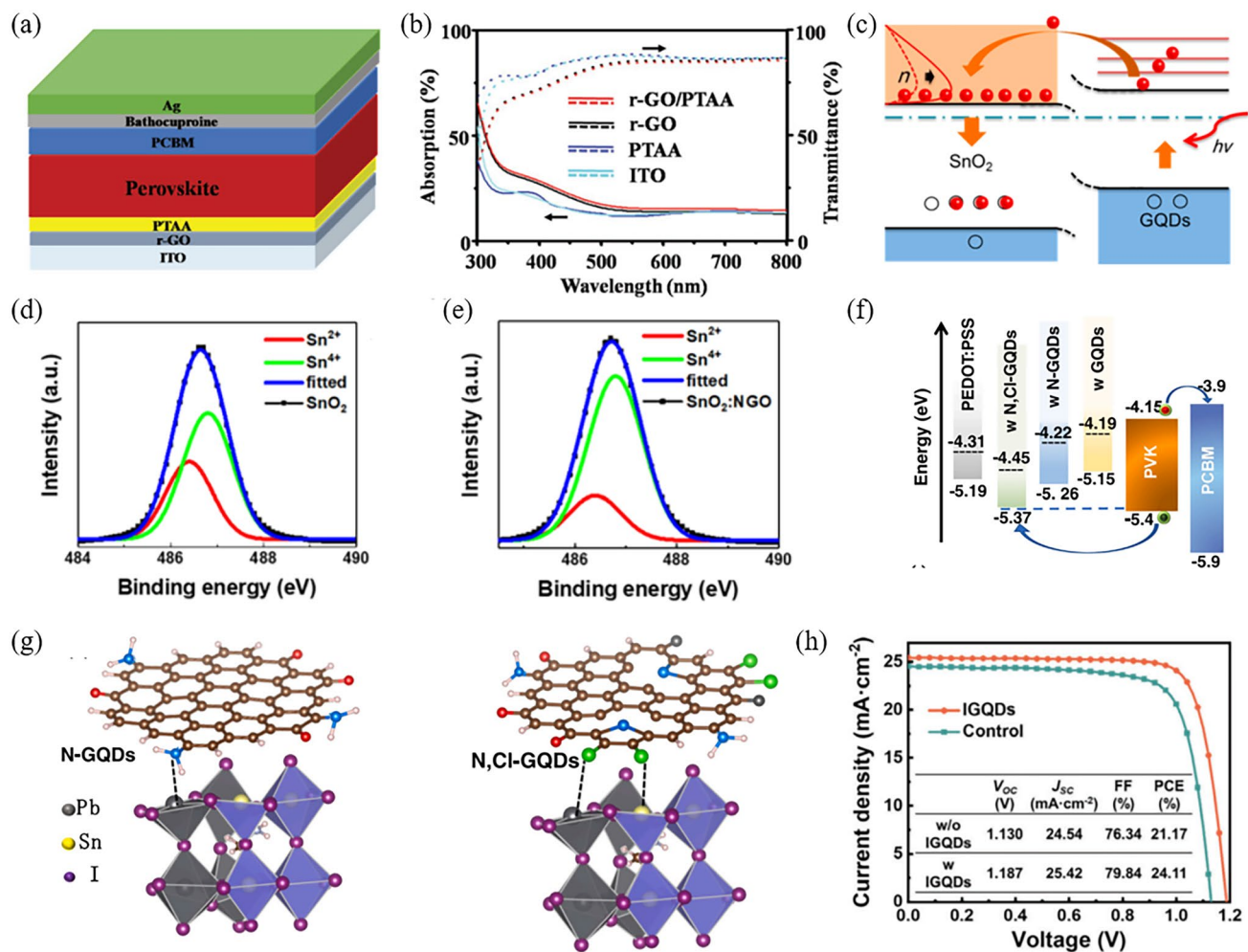
Fig. 3 **a** Diagram of the device with a bilayer hole transport system of rGO/PTAA. **b** The absorption and transmission spectra of ITO, PTAA, rGO, and rGO/PTAA. Reproduced with permission from Ref. [78]. Copyright 2017, Wiley. **c** Schematic illustration of the process of hot electron transfer from GQDs to SnO$_2$ under illumination. Reproduced with permission from Ref. [134]. Copyright 2017, American Chemical Society. **d, e** X-Ray Photoelectron Spectroscopy of the Sn 3d$_{5/2}$ peak acquired from **d** the pristine SnO$_2$ layer and **e** the composite layer of SnO$_2$:NGO. Reproduced with permission from Ref. [133]. Copyright 2020, American Chemical Society. **f** Energy level diagram of device components. **g** Schematic illustration of N passivation for under-coordinated Pb and Cl passivation for under-coordinated Pb/Sn in the perovskite. Reproduced with permission from Ref. [124]. Copyright 2022, Elsevier. **h** Current–voltage (*J-V*) curves of the devices with and without I-GQDs. Reproduced with permission from Ref. [123]. Copyright 2023, Wiley

MAPbI$_3$-based PSC increased from the initial 18.12% to 20.55%, with an improved V_{OC} from 1.08 to 1.12 V.

On the other hand, the bottom interface undergoes severe compressive or tensile strain during the thermal annealing process, as the thermal expansion coefficient of perovskite is approximately ten times higher than that of the underlying metal oxide layer [138–140]. This residual stress not only hampers carrier transport but also accelerates the aging process of the device. In particular, the all-inorganic CsPbBr$_3$ material exhibits a phase transform temperature of up to 250 °C, which is higher than its traditional hybrid perovskite

counterpart [141]. This notable difference in temperature gradient is expected to result in an increased tensile strain at the bottom interface. To mitigate this problem, a vdW heterostructure composed of WS$_2$/CsPbBr$_3$ has been demonstrated [51]. In this situation, WS$_2$ acts as a lubricant between CsPbBr$_3$ and the metal oxide substrate, thereby alleviating the constraints imposed by the substrate on the expansion and contraction of the perovskite lattice. The cross-sectional energy-dispersive spectroscopy mapping images demonstrate that the migration of ions at interfaces is significantly suppressed due to enhanced interface contact and improved
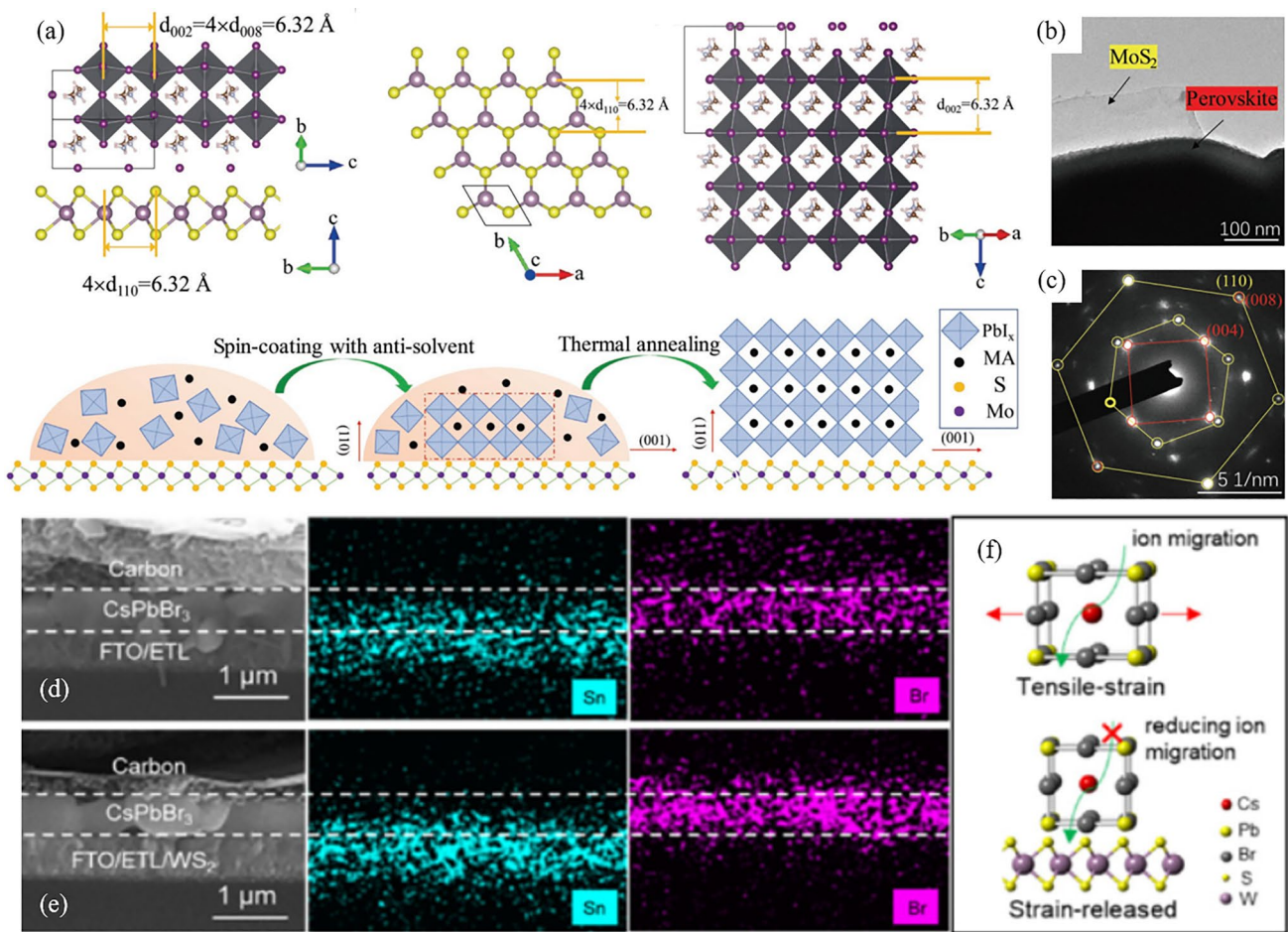
Fig. 4 **a** Schematic illustration of the vdW epitaxial growth of a MAPbI$_3$ grain on a MoS$_2$ surface. The interplanar distances of the MoS$_2$ (110) and MAPbI$_3$ (008) planes are identical, which is perfect for epitaxial growth. **b** Top-view transmission electron microscopy image of MoS$_2$ with a MAPbI$_3$ perovskite layer grown on its surface. **c** The selected-area electron diffraction pattern of an overlapping area of MAPbI$_3$ and MoS$_2$. Two separate diffraction spots are observed: the yellow one belongs to MoS$_2$, while the red one belongs to MAPbI$_3$. Reproduced with permission from Ref. [111]. Copyright 2019, Wiley. **d, e** Cross-sectional scanning electron microscopy images and their corresponding energy dispersive spectroscopy mapping images of CsPbBr$_3$ PSCs **d** without and **e** with WS$_2$ modification after aging treatment. **f** Schematic illustration of ion migration in tensile strain- and strain-released perovskite unit cells. Reproduced with permission from Ref. [51]. Copyright 2020, Wiley

perovskite lattice structure (Fig. 4d-f). Moreover, the average decay time of electrons decreased from 0.575 ns (without WS$_2$) to 0.247 ns (with WS$_2$). As a result, the PCE of all-inorganic PSCs with an FTO/SnO$_2$-TiO$_x$Cl$_{4-2x}$/WS$_2$/CsPbBr$_3$/carbon structure has reached 10.65%, with V_{OC}, J_{SC}, and FF of 1.70 V, 7.95 mA cm^{-2}, and 79%, respectively. As a comparison, the PCE of the pristine device is 9.27%, with V_{OC}, J_{SC}, and FF of 1.59 V, 7.45 mA cm^{-2}, and 78.3%, respectively. Moreover, WS$_2$ has been employed to modify the interface between the PTAA and the ternary cation perovskite (Cs$_{0.05}$MA$_{0.05}$FA$_{0.9}$PbI$_{2.7}$Br$_{0.3}$) [118]. Here, the researchers prepared WS$_2$ nanosheets with an average lateral size of 700 nm and a thickness ranging

from 2–5 nm. These nanosheets demonstrated an optical bandgap of 1.76 eV, with a VBM of −5.12 eV and a CBM of −3.36 eV. These energy levels are well-aligned with the energy levels between PTAA and the perovskite film. In addition, the lattice distance on the (020) plane of the Cs$_{0.05}$MA$_{0.05}$FA$_{0.9}$PbI$_{2.7}$Br$_{0.3}$ is 0.31 nm, which is twice that of the (110) plane of WS$_2$. This characteristic enhances the compatibility between the two materials and promotes the vdW epitaxial growth of Cs$_{0.05}$MA$_{0.05}$FA$_{0.9}$PbI$_{2.7}$Br$_{0.3}$ atop WS$_2$. As a result, the defect state density of the perovskite film was reduced from 1.94×10^{15} to 0.68×10^{15} cm^{-3}. With the remarkable enhancement in V_{OC} from 1.08 to 1.15 V, the WS$_2$-based PSC achieved a PCE of 21.1%, which is

one of the highest reported PCEs for inverted PSCs at that time. For Sn-based perovskites ($FASnI_3$), the utilization of MoS_2, WS_2, and WSe_2 as templates has been demonstrated to effectively promote vdW epitaxial growth and produce larger crystalline grains. However, among the three templates, WSe_2 exhibits the highest VBM, which aligns more favorably with the VBM of $FASnI_3$. Consequently, photovoltaic devices incorporating WSe_2 templates yield the highest photovoltaic performance.

Expect for the application in inverted PSCs, metal sulfides can also be utilized in the bottom interface of regular PSCs. For example, SnS_2 is a typical binary 2D material with n-type semiconductor properties [142, 143]. It has a bandgap of ~ 2.5 eV, with VBM and CBM of −6.54 and −4.24 eV, respectively. Compared to SnO_2 ETL, 2D SnS_2 film displays a superior electron mobility (7.85×10^{-4} vs 9.78×10^{-5} cm^2 V^{-1} s^{-1}), a higher conductivity (7.17×10^{-4} vs 1.78×10^{-5} S cm^{-1}), and a lower root mean square roughness (RMS, 0.31 vs 2.4 nm). By replacing SnO_2 with SnS_2 as the ETL, the loss caused by the imbalance of charge carriers at the ETL/perovskite and perovskite/HTL interfaces is significantly reduced. Due to the enhancements in V_{OC} (1.095 to 1.161 V) and J_{SC} (22.60 to 23.55 mA cm^{-2}), the PCE of SnS_2-based PSCs improved from 17.72% to 20.12% [144]. This achievement establishes the highest PCE for PSCs using SnS_2 as the ETL. In a recent breakthrough, an all-in-one SnO_2-SnS_2-$CsPbBr_3$ interface, with architecture of SnS_2 [0.316 nm for (100)]/SnO_2 [0.335 nm for (110)] and SnS_2 [0.589 nm for (001)]/$CsPbBr_3$ [0.587 nm for (001)] directions, was established [112]. Here, SnS_2 functions as a "bridge" between the incompatible interface of SnO_2 ETL and $CsPbBr_3$ active layer. This exquisite design diminishes the interface barrier, thereby minimizing energy loss as charges traverse the interface. Besides, due to the matched lattice and high-quality epitaxial growth, the defect density of $CsPbBr_3$ thin films decreased from 1.80×10^{16} to 1.41×10^{16} cm^{-3}. Through this all-in-one strategy, the all-inorganic, carbon electrode-based $CsPbBr_3$ PSC exhibits a boosted PCE of 10.72%, along with an enhanced V_{OC} of 1.635 V. After being stored in air at 80% relative humidity (RH) and 25 °C for 700 h, the unencapsulated device retains 90% of its initial PCE.

3.3 MXenes

The MXenes, a rapidly expanding family of 2D materials, are well-known for their unique optoelectronic properties

and adjustable surface termination [94, 145]. $Ti_3C_2T_x$ is the first discovered MXenes, which exhibits metallic conductivity, flexibility, hydrophilicity, and an oxide-like surface termination [146]. Notably, UV-ozone treatment is an important approach to enhance the electronic properties of $Ti_3C_2T_x$. For a regular device utilizing $Ti_3C_2T_x$ as the ETL, the initial performance was characterized by a modest PCE of 5.00%, with a V_{OC} of 0.8 V, J_{SC} of 15.87 mA cm^{-2}, and FF of 40%. Interestingly, after 30 min of UV-ozone treatment on $Ti_3C_2T_x$, the PCE substantially improved to 17.17%, with an enhanced V_{OC} of 1.08 V, J_{SC} of 22.63 mA cm^{-2}, and FF of 70% [147]. The X-ray photoelectron spectroscopy indicates that UV-ozone treatment increases the Ti–O bonds on the surface of $Ti_3C_2T_x$, thereby reducing the non-radiative recombination losses at the $Ti_3C_2T_x$/perovskite interface. Recently, research has shown that $Ti_3C_2T_x$ can be used as an additive or passivation layer to improve the interfacial contact between SnO_2 and the perovskite layer. For example, by doping a small amount of $Ti_3C_2T_x$ into SnO_2, the vdW interaction between SnO_2 nanocrystals is weakened. This refinement leads to an optimized ETL exhibiting an impressive boost in conductivity from 9.62×10^{-5} to 1.85×10^{-4} S cm^{-1} [125]. In addition, the as-prepared SnO_2-$Ti_3C_2T_x$ composite layer promotes the vertical crystal growth of perovskite, with the average grain size increasing from ~ 356 nm to 1 μm (Fig. 5a). As a result, the PCE of the SnO_2-$Ti_3C_2T_x$ device enhanced from the initial 20.03%, with V_{OC}, J_{SC}, FF of 1.09 V, 24.16 mA cm^{-2}, 75.8%, respectively, to 23.07%, with V_{OC}, J_{SC}, FF of 1.13 V, 25.07 mA cm^{-2}, 81.1%, respectively. In a similar device, by introducing $Ti_3C_2Cl_x$ as a passivation layer between the SnO_2 and perovskite layer, the device achieved a high PCE of 24.86%, with V_{OC} increasing from 1.173 to 1.203 V and FF rising from 78.05% to 82.14% [127]. This improvement is mainly attributed to the anchoring of Pb^{2+} by Cl_x terminals. Despite its excellent performance, $Ti_3C_2T_x$ is prone to agglomeration, which limits its application in large-area PSCs. In order to address this challenge, a unique MXene/Glucose/PEDOT:PSS nanocomposite HTL has been proposed for flexible large-area perovskite solar module [126]. The incorporation of glucose and its half-caramelization process facilitate the spontaneous exfoliation and redistribution of aggregated $Ti_3C_2T_x$ MXene nanosheets within PEDOT:PSS (Fig. 5b). Based on this strategy, the flexible perovskite solar minimodule (15 cm^2) achieved a high PCE of 17.06% and demonstrated excellent repeatability (Fig. 5c–d). After 1000 h of continuous 1-sun
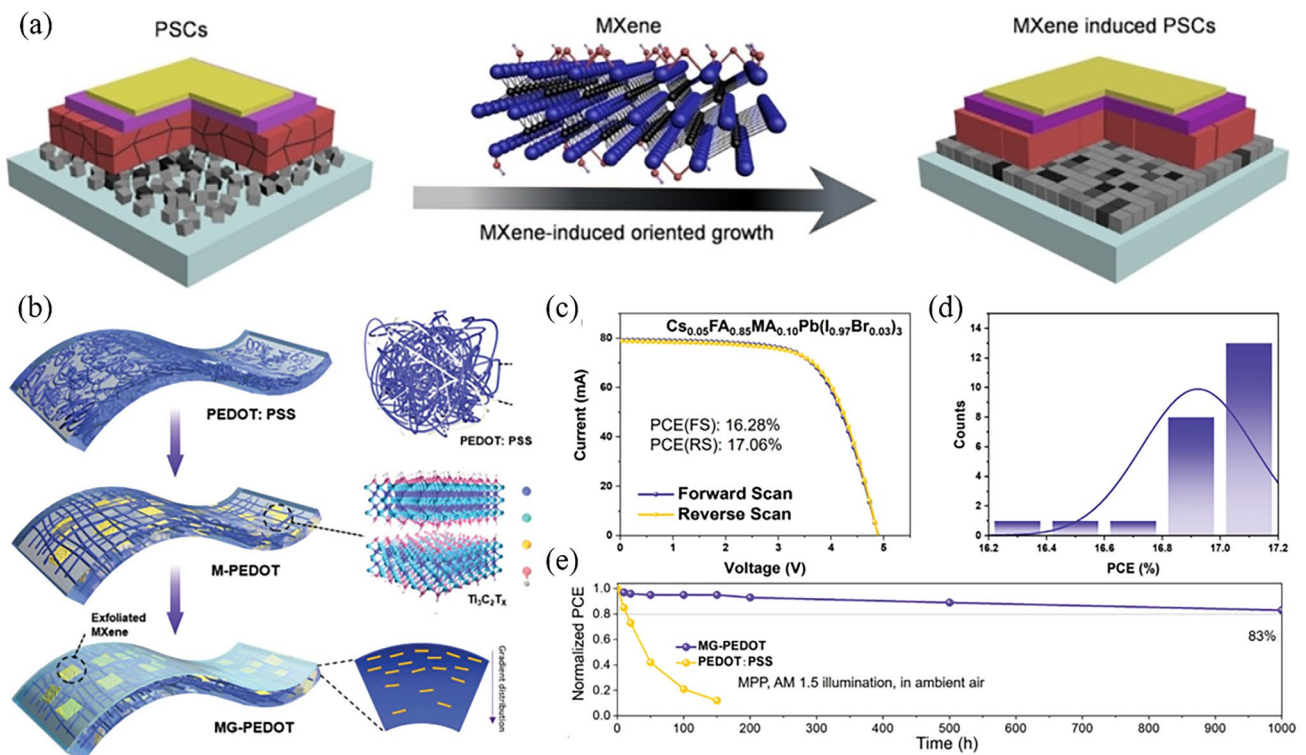
Fig. 5 **a** Structural model of the vertical growth of perovskite induced with MXene. Reproduced with permission from Ref. [125]. Copyright 2022, Wiley. **b** Schematic illustration of the nanocomposite MG-PEDOT film preparation. **c-e** Photovoltaic performance of flexible modules based on MG-PEDOT. **c** *J–V* curves. **d** Efficiency statistics of 24 separate perovskite solar modules. **e** The stability of encapsulated devices under operational conditions (AM 1.5 illumination) in ambient air. Reproduced with permission from Ref. [126]. Copyright 2023, Wiley

illumination, their initial PCE is retained at 83% while performing maximum power point tracking (Fig. 5e).

In comparison to $Ti_3C_2T_x$, Nb_2CT_x has a larger surface area, which can be attributed to the absence of one atomic layer [148]. This advantage enhances the contact area with perovskite, thereby facilitating the extraction and transport of carriers. Additionally, the plentiful surface groups, including -OH, -O, -F, and $-NH_2$, can be readily integrated into Nb_2CT_x MXene [93]. Theoretical calculations have shown that the WF of O-terminated Nb_2CT_x MXene is higher than that of OH-terminated counterparts [149]. The researchers conducted a treatment of Nb_2CT_x with O plasma, which led to an observed increase in its WF from 4.7 to 5.04 eV. Using this as the HTL in an inverted PSC resulted in an enhancement of the PCE from 18.08% to 20.74% [150]. Conversely, when hydrazine (N_2H_4) is used, it replaces the surface -F groups with $-NH_2$ groups, resulting in a reduction of the WF of Nb_2CT_x from 4.65 to 4.32 eV. Furthermore, the existence of a dipole moment from the Nb layer to the $-NH_2$ groups leads to an upward shift of the VBM of Nb_2CT_x.

This adjustment allows the VBM of Nb_2CT_x to align with that of the perovskite layer. As a result, a considerable PCE of 21.79% has been achieved in a regular PSC that employs Nb_2CT_x as the ETL [128]. Besides, the corresponding flexible and large-area (active area of 0.99 cm^2) counterparts achieve PCEs of 19.15% and 18.31%, respectively. Due to the inhibition of I^- migration by $-NH_2$ groups, this type of PSC demonstrates excellent stability. The unencapsulated device retains 93% of its initial PCE after being stored for 1,500 h inside a glovebox.

3.4 Black Phosphorus and Other 2D Materials

As an emerging 2D material, BP possesses a tunable direct bandgap and ambipolar conductivity characteristics [151, 152]. In its polycrystalline form, BP demonstrates impressive electron and hole mobility, with levels as high as 220 and 350 cm^2 V^{-1} s^{-1}, respectively [153]. It is worth noting that the electron mobility of traditional TiO_2 is only 0.1–4

$cm^2 V^{-1} s^{-1}$, which is approximately three orders of magnitude lower than that of BP [154]. Therefore, replacing TiO_2 with BP as the ETL in PSCs is a logical progression. This approach becomes even more advantageous with the promising potential of BP in low-temperature solution-based synthesis, especially for the production of flexible PSCs. For example, through the implementation of the liquid-phase exfoliation technique, the researchers synthesized BP quantum dots (BPQDs) with a diameter distribution ranging from 3 to 10 nm. These BPQDs were then utilized as the ETL in a flexible PSC. After the optimization of the number of BPQD layers (5-layers), the device PEC increased from 3.58% (without BPQDs) to an impressive 11.26% (with BPQDs) [155]. Moreover, recent research revealed that the incorporation of a small amount of BPQDs in CsFAMA perovskite can raise its energy barrier for defect formation, which is supported by the observed reduction in defect state density from 2.83×10^{16} to 8.96×10^{15} cm^{-3}. Benefitting from it, the PCE of the PSC incorporating of BPQDs improved from 19.13% to 22.85% as its V_{OC} was enhanced from 1.17 to 1.22 V [156]. Notably, the V_{OC} ranks among the highest values for perovskite film with a bandgap of ~ 1.60 eV.

Besides the utilization as an ETL, the bipolar transport nature of BP also makes it a popular option for modifying the HTL. For instance, remarkable enhancements in performance have been achieved by incorporating phosphorene nanoribbons (PNRs) as charge-selective interlayers at the PTAA/MAPbI$_3$ interface (Fig. 6a) [130]. The hole extraction time was reduced from 15.5 to 9.9 ns, while the conductivity of HTL witnessed an enhancement from 9.25×10^{-7} to 1.02×10^{-6} S cm^{-1} (Fig. 6b, c). This modulation has resulted in a high FF of 83% for the corresponding inverted PSCs, with an PCE exceeding 21%. Moreover, it has been found that the bandgap and conduction structure of BP can be facilely tuned by manipulating the spin-coating times of BP dispersion on the substrates [129]. Building upon this understanding, researchers designed an device that incorporates a cascade conduction band at both the ETL/perovskite and perovskite/HTL interfaces (Fig. 6d). This innovative approach improved charge extraction and boosted the overall performance of the device.

Besides, other 2D materials such as antimonene, h-BN, CNs, and MOFs have been reported for the modification of the bottom interface of PSCs [67, 68, 158, 159]. Among them, antimonene seems to have great application prospects. Antimonene is a 2D material similar to BP in terms of properties, while demonstrates exceptional stability in both its physical and chemical characteristics [99]. Theoretical calculations indicate that as antimonene transitions from bulk to monolayer, its material properties undergo a transformation from semimetallic to semiconducting. Throughout this process, the band gap of antimonene increases from 0 to ~ 2.28 eV [101]. Furthermore, the semiconducting form of antimonene exhibits high carrier mobility, exceptional thermal conductivity, and spin-electronic properties [160, 161]. However, the production of high-quality, large-area thin antimonene layers has been challenging in experiment due to the short interlayer distance and high binding energy of antimonene. In order to address this issue, a method has been developed that includes a pre-grinding step, followed by liquid-phase exfoliation aided by sonication (Fig. 6e) [157]. By subjecting the mortar to pre-grinding, a shear force is applied along the surfaces of the layers. This process facilitates the formation of large, thin antimony plates, which can be conveniently exfoliated into smooth and sizable antimonene sheets. When the as-prepared antimonene was utilized as the HTL in PSCs, the J_{SC} of the corresponding devices increased from 11.2 (in the absence of an HTL) to 14.6 mA cm^{-2}. Encouragingly, the incorporation of a monolayer of antimonene between PTAA and MAPbI$_3$ yielded an augmentation in J_{SC} from 21.69 to 23.52 mA cm^{-2} [67]. These findings confirm the rapid extraction and efficient hole transportation abilities of antimonene, establishing it as a promising candidate for future high-performance PSCs.

4 2D Materials at Top Interfaces

The top interface refers to the interface between the perovskite layer and the back electrode. For a regular device, the top interface includes the interfaces of perovskite/HTL and HTL/back electrode. Therefore, the top interface extracts photogenerated holes from the active layer while obstructing the backflow of electrons [25, 26]. On the other hand, the top interfaces of inverted device have an opposite configuration and direction of charge transport. Unlike the bottom interface, the top interface does not exert a direct influence on the light absorption and film quality of the perovskite layer. However, the rapid crystallization and ionic nature of perovskite materials give rise to numerous defects on its surface, including dangling bonds, voids, and free charges, which limit the efficiency and stability of the PSCs [30, 162]. Additionally, due to the lack
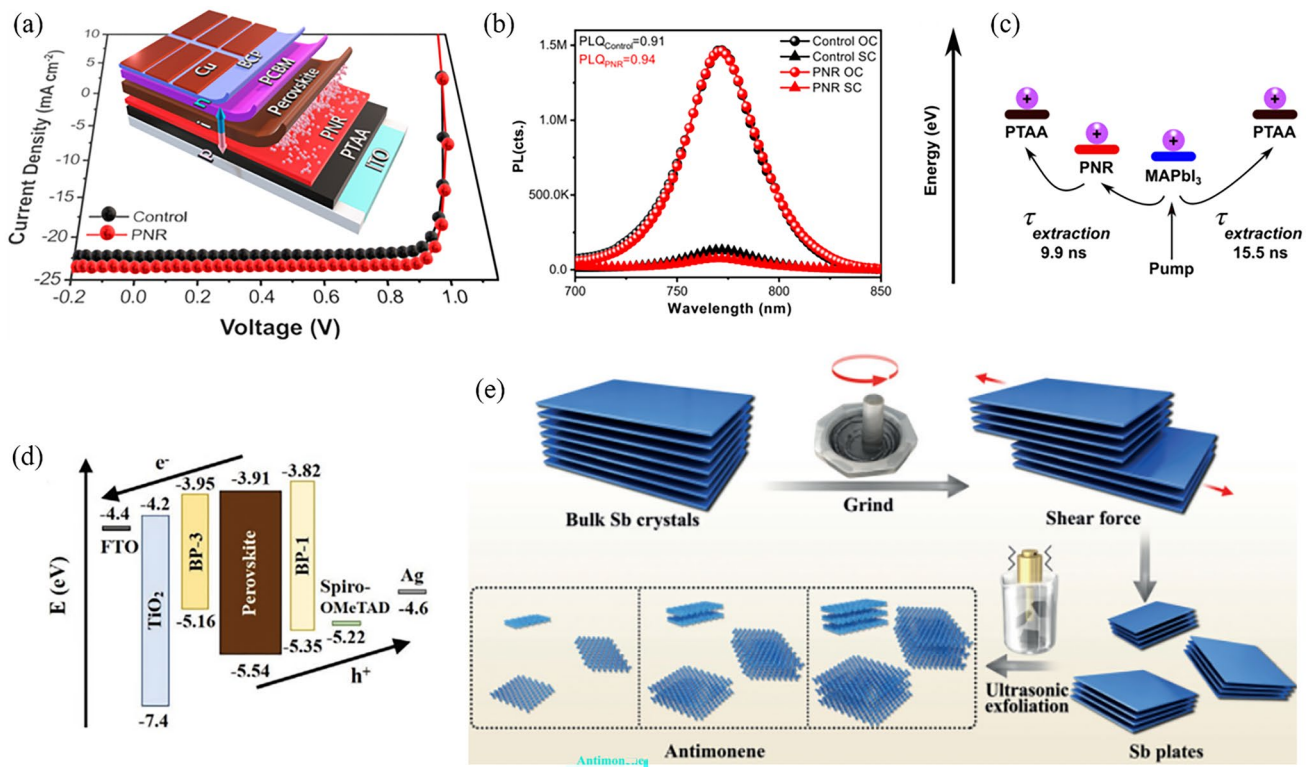
Fig. 6 **a** Schematic diagram of PNRs-modified inverted PSC and the corresponding *J-V* curves. **b** Photoluminescence of control and PNRs devices under open-circuit and short-circuit conditions. **c** Proposed diagram of enhanced hole extraction facilitated by PNRs. Reproduced with permission from Ref. [130]. Copyright 2021, American Chemical Society. **d** Energy level diagram of each constituent in PSC with dual-positioning of BP at both interfaces. Reproduced with permission from Ref. [129]. Copyright 2020, Wiley. **e** Schematic illustration of the fabrication process for antimonene. Reproduced with permission from Ref. [157]. Copyright 2018, Wiley

of isolation from bulk perovskite, the top interface is more vulnerable to external stimuli such as water, oxygen, and heat. Besides, the chemical reactions occurring at the top interface, which involve the migration of halide anions and the diffusion of metal atoms, result in severe degradation of the perovskite materials [36, 48, 50]. Taking into account these considerations, the incorporation of buffer layers at both the interfaces between the perovskite and CTLs, as well as between the CTLs and the back electrode, is an important strategy to enhance the PCE and stability of the PSCs. The hydrophobicity, compactness, and chemical stability of these interfacial materials play a pivotal role in the success of this approach. In Sect. 4, we summarize the utilization of 2D materials at the top interface of PSCs, focusing on their roles as an active buffer layer (ABL) and interlayer. Representative 2D materials at top interface for the enhancement of device performance and stability are illustrated in Table 3.

4.1 Graphene and Its Derivatives

In contrast to the bottom interface, the modification of the top interface is considered a post-treatment technique, as it occurs after the crystallization of the perovskite layer has been completed. Due to its remarkable compactness and chemical inertness, the incorporation of graphene and its derivatives as an interlayer material between the perovskite and the back electrode significantly enhances the operational stability of PSCs. For example, researchers replaced the expensive 2,2',7,7'-tetrakis(N,N-p-dimethoxyphenylamino)-9,9'-spirobifluorene (spiro-OMeTAD) with inorganic copper(I) thiocyanate (CuSCN)/rGO to construct devices with a structure of FTO/TiO$_2$/CsFAMAPbI$_{3-x}$Br$_x$/CuSCN/rGO/Au and achieved comparable PCE with the spiro-OMeTAD-based counterpart (20.8% vs 20.4%) [48]. In this case, rGO acts as an ABL

Table 3 Representative 2D materials at the top interface for improving the efficiency and stability of PSCs

2D materials	Device structure	PCE (%)	Characteristic and stability	Function	Refs
Graphene	FTO/SnO$_2$/FAPbI$_3$/spiro-OMeTAD/EVA/graphene/Cu-Ni/graphene	24.34	95% its initial PCE after 5,000 h of tracking at maximum power points under continuous 1-sun illumination	Inhibit ion migration metal diffusion, energy level alignment	[36]
Oxo-Graphene	ITO/MeO-2PACz/CsFAMA:Oxo-Graphene/C$_{60}$/BCP/Ag	23.7	93.8% its initial PCE after 1,000 h of tracking at maximum power points under continuous 1-sun illumination	Provide anchoring sites to bind the excess PbI$_2$ in perovskite, passivate grain boundaries	[163]
rGO	FTO/TiO$_2$/CsFAMA/CuSCN/rGO/Au	20.4	All-inorganic HTL, > 95% its initial PCE after 1000 h of tracking at maximum power points under continuous 1-sun illumination at 60 °C	As a spacer layer, suppress potential-induced degradation of the CuSCN/Au contact	[48]
Cl-GO	ITO/SnO$_2$/FAMAPbI$_3$/Cl-GO/PTAA/Au	21.08	Active area of 1.02 cm^2, 90% of its initial PCE for 1,000 h under 1-sun of illumination at 60 °C	Form strong Pb–Cl and Pb–O bonds, impede the loss of decomposed components from soft perovskites	[50]
Ti$_1$-rGO	FTO/c-TiO$_2$/mp-TiO$_2$/CsFAMA/spiro-OMeTAD/Ti$_1$-rGO/FTO	21.6	98% and 95% of its initial PCE for 1,300 h under 1-sun of illumination at 25 and 60 °C, respectively	Improve electrical contact of interface, energy level alignment	[52]
QD/GO	ITO/SnO$_2$/perovskite/(QD/GO)/spiro-OMeTAD/Au	18.55	Minimodule (36 cm^2), 90% of its initial PCE for 1,000 h under 1-sun of illumination at 60 °C, in ambient air	Improve charge transport, suppress ion and moisture diffusion	[164]
MoS$_2$	FTO/c-TiO$_2$/SnO$_2$/CsFAMA/MoS$_2$/PTAA/Au	18.54	Dopant-free HTL, 80% of its initial PCE for 45 h under 1-sun of illumination with 45%–50% RH, at room temperature, unencapsulated	Suppress interfacial charge accumulation, serve as a complementary layer to the dopant-free HTL	[165]
WS$_2$	FTO/TiO$_2$/CsPbBr$_3$/WS$_2$/AgIn$_5$S$_8$/Carbon	10.24	All-inorganic, over 93% of its initial PCE after being stored in air with high humidity and temperature (85% RH, 85 °C) for 720 h	Function as HTL, building a convenient pathway for hole transport via Pb–S–W bonds	[166]
SnS$_{1-x}$O$_{2x}$	ITO/SnO$_2$/CsFAMA/(BA)$_2$PbI$_4$/SnS$_{1-x}$O$_{2x}$/spiro-OMeTAD/Au	24.5	94.5% of its initial PCE after being stored in air with 20%–40% RH for 720 h	Promote carrier transport via Sn-I bonds, enhance the conductivity and hydrophobicity of HTL	[167]
F-BP	FTO/c-TiO$_2$/mp-TiO$_2$/CsFAMA/F-BP/spiro-OMeTAD/Au	22.06	95% of its initial PCE after 30 days storage with 50% RH at room temperature, unencapsulated	Mitigate the density of trapped states, enhances antioxidant and moisture resistance	[168]
BPQDs	FTO/SnO$_2$/CsFAMA/Cs$_3$TbCl$_6$QDs/spiro-OMeTAD:BPQDs/Au	23.49	88% of its initial PCE after 2,520 h in ambient air with 30% RH, unencapsulated	Improve the hole mobility and conductivity of HTL	[169]
g-C$_3$N$_4$	PDMS/PEDOT:PSS/FASnI$_3$:g-C$_3$N$_4$/C$_{60}$/BCP/Ag	8.56	91% of its initial PCE after 1,000 h in N$_2$ environment; 92% of its initial PCE after 600 cycles at a curvature radius of 3 mm	Delay crystallization, enhance hydrophobicity and oxidation resistance	[69]
Ti$_3$C$_2$T$_x$	ITO/PTAA/CsPbI$_3$/Ti$_3$C$_2$T$_x$/CPTA/BCP/Ag	19.69	85% of its initial PCE for 1,000 h under 1-sun of illumination with 85% RH and 85 °C	Strengthen the electric field at the perovskite/ETL interface, improve charge separation	[170]
Nb$_2$CT$_x$	FTO/SnO$_2$/Nb$_2$CT$_x$/CsFAMA/Nb$_2$CT$_x$/spiro-OMeTAD/Ag	24.11	93% its initial PCE after 1,500 h test under an ambient condition with 10%–20% RH	Energy levels offsets reduction, conduct hole current from grain boundaries to the HTL	[171]

that inhibits the diffusion of ions and metals at the top interface. Combined with the stability of CuSCN, the PSC containing rGO was maintained at 95% of the initial PCE after aging for 1,000 h at the maximum power point under 1-sun illumination and at a temperature of 60 °C. In contrast, the PSC without rGO exceeded 50% of PCE loss. In recent advancements, a composite electrode of copper–nickel (Cu–Ni) has been reported to replace the noble metal electrodes. This alloy is encapsulated with in situ grown bifacial graphene, which improves the stability of the electrode and aligns its energy levels with those of the HTL. The resulting device achieved a high PCE of 24.34% and exhibited 5,000 h operational stability at the maximum power point under continuous 1-sun illumination (Fig. 7f) [36]. Although the favorable performance exhibited by small-area PSCs, they still face challenges when it comes to scaling up from laboratory cells to industrial modules [28, 172]. It has been observed that scalable fabrication can result in increased defects, pinholes, impurities, and deficient contact areas at the interfaces. These detrimental outcomes trigger an amplified leakage current and non-radiative recombination, which compromise the efficiency and long-term stability of the PSCs [173, 174]. To tackle this concern, a strategy of synergistic interface modulation has been proposed by crosslinking CsPbBr$_3$ quantum dots (QDs) and conductive GO through a Pb–O bond [164]. The ensuing composite (GO/QDs) show a uniform distribution on the large scan, which offer unparalleled charge transport and efficient interfacial passivation (Fig. 7a). Additionally, the time-of-flight secondary ion mass spectroscopy depth profiles indicate that the GO/QDs interlayer serves as a reliable barrier to hinder the diffusion of ions and metal at the top interface (Fig. 7b). As a result, the PCE of the minimodules (area of 17.11 cm^2) has witnessed an enhancement from 16.56% to 18.55%. The certified steady-state PCE of this device reaches 17.85%, positioning it among the highest certified efficiencies for minimodule PSCs. After exposure to continuous irradiation of 1-sun for a duration of 1,000 h at 85 °C and 60% RH, the module PCE remains at a remarkable 91%.

In order to make GO more closely combine with perovskite and CTL, doping with heteroatoms such as chlorine and fluorine is essential. For example, by introducing a layer of chlorinated GO (Cl-GO) between perovskite and PTAA, the researchers constructed a perovskite/Cl-GO/HTL heterojunction, and compared it with GO and control (without interlayer) samples [50]. On an aperture area of 1.02 cm^2,

the PCEs of the three devices were 20.00% (control), 20.29% (GO), and 21.08% (Cl-GO), respectively. After operating at the maximum power point for 1,000 h at 60 °C, the PCE of the Cl-GO device remains 90%, whereas the control cell and the cell with GO experienced reductions of 65% and 50%, respectively. This improvement is attributed to the formation of strong Pb-Cl and Pb–O bonds, which reduces the barrier at the top interface (Fig. 7c-e). Furthermore, the use of fluorinated graphene (FG) as an additive in spiro-OMeTAD has been shown to have a versatile impact on improving the performance of PSCs [175]. Firstly, the p-type features of graphene have been strengthened due to the incorporation of highly electronegative fluorine. Secondly, the 2D network structure of FG has the ability to eliminate existing pinholes in spiro-OMeTAD and enhance its hydrophobic properties. This enhancement helps to increase the device resistance to moisture in the air. Finally, the introduction of impurity atoms disrupts the inherent structure of graphene, which leads to an increased number of adsorption sites. As a result, the FG modified PSC achieves a PCE of 23.14%, which surpasses the control device by 11.8%. After a 2,400 h operation under ambient conditions with 25% RH, this graphene-enhanced device retains 90% of its initial PCE.

Although GO offers numerous benefits for charge extraction and device protection, it also poses a notable challenge due to the oxygen-containing functional groups on its surface. These groups serve to extract holes but localize charges, leading to a conflict in maximizing both hole extraction and charge transfer [176]. To address this issue, an inorganic nanomaterial, (NiCo)$_{1-y}$Fe$_y$O$_x$ nanoparticles, has been utilized as a modifier for GO (denoted as NP-GO) [177]. Based on the disparity in electronegativity, electrons from the oxygen-containing groups will spontaneously transfer to the inorganic NPs. This phenomenon results in the p-doped GO and induces surface-oriented dipole motion (Fig. 8a). Consequently, the enhanced hole extraction of GO leads to a reduction in charge recombination loss at the perovskite/HTL interface, which is supported by the surface potential patterns of the top interfaces (Fig. 8b, c). As a result, the all-inorganic PSC fabricated using the structure of FTO/c-TiO$_2$/CsPbIBr$_2$/NP-GO/carbon has reached a PCE of 10.95%. This represents a notable improvement of 7.38% compared to the reference cell. Due to the protective effect of NP-GO, this device retains 90% of its initial PCE even after being subjected to 70 days of aging in 10% RH air conditions. Recently, a chemisorption method has
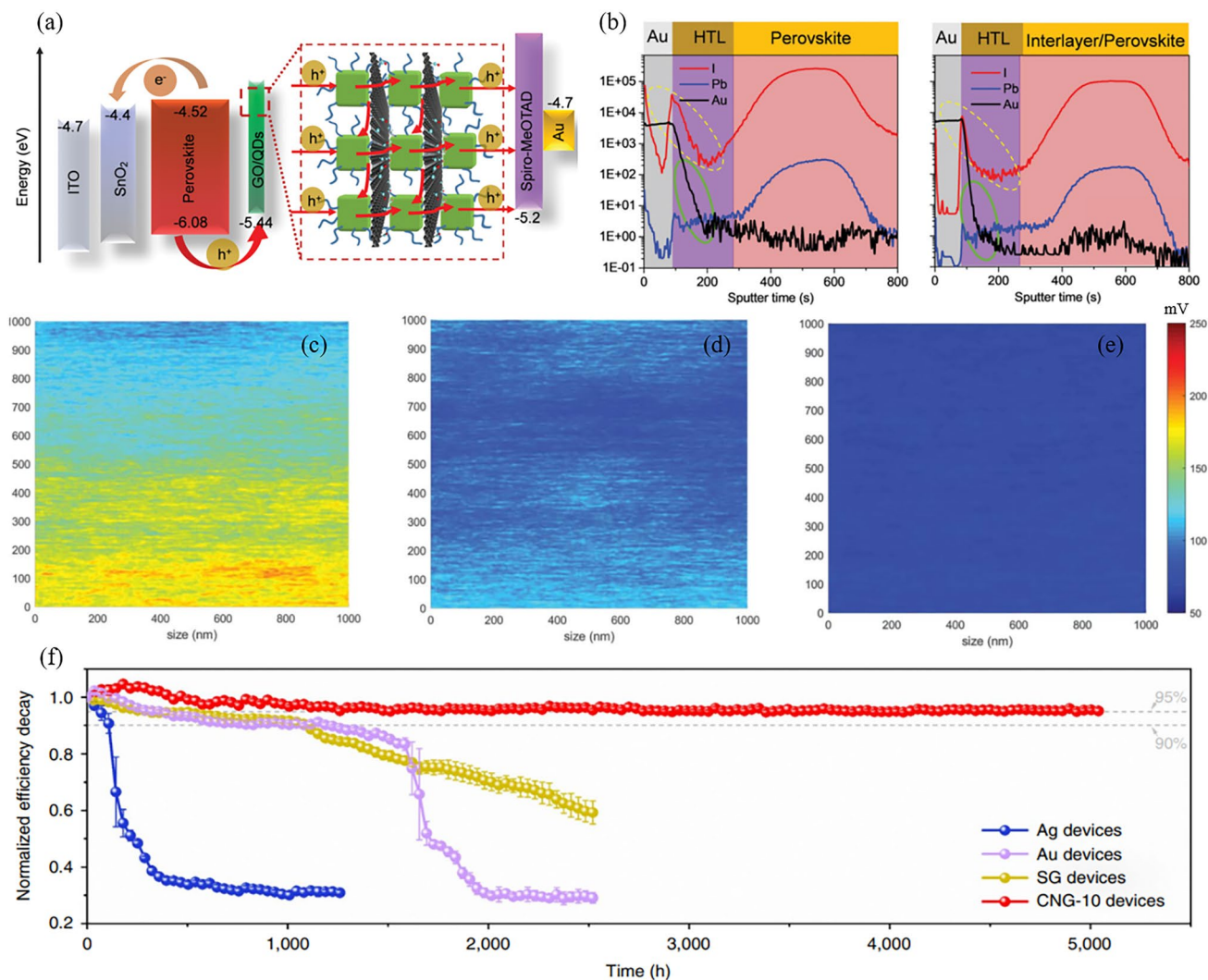
Fig. 7 a Schematic illustration of the energy levels and charge transport mechanism of PSC with a GO/QDs interlayer. **b** Time-of-flight secondary ion mass spectroscopy depth profiles of iodide ion, Au, and Pb distribution in PSCs without and with the GO/QDs interlayer. Reproduced with permission from Ref. [164]. Copyright 2022, The Royal Society of Chemistry. **c–e** Potential mapping images of **c** perovskite/PTAA, **d** perovskite/GO/PTAA, and **e** perovskite/Cl-GO/PTAA measured by kelvin probe force microscope. Reproduced with permission from Ref. [50]. Copyright 2019, AAAS. **f** The operational stability of PSCs with different electrodes at the maximum power point under one sun illumination. The SG and CNG-10 represent the control sample and the Cu–Ni alloy protected by graphene with 10 layers, respectively. Reproduced with permission from Ref. [36]. Copyright 2022, Springer Nature

been employed to introduce a single titanium (Ti) atom onto the surface of rGO, which leads to the formation of a single-atom material (SAM) of Ti_1-rGO [52]. In this particular case, the Ti adatoms were anchored to the rGO surface through oxygen atoms. By employing density functional theory calculations, noticeable charge transfer between rGO and Ti adatoms has been revealed (Fig. 8d). This phenomenon leads to a decrease in the Fermi level of rGO from -4.05 to -4.31 eV, which is better matched with that of spiro-OMeTAD (-4.25 eV) (Fig. 8e). By incorporating Ti_1-rGO

as the back electrode in carbon-based PSCs (C-PSCs), the series resistance, interfacial contact, and band alignment mismatch between the carbon electrode and adjacent functional layer are minimized. Consequently, the V_{OC} and FF of the C-PSCs increased from their initial values of 0.998 V and 25.6 mA cm^{-2} to improved levels of 1.059 V and 26.0 mA cm^{-2}, respectively. In line with this, the PCE of the device experiences a significant increase, rising from 17.7% to 21.6%, approaching the PCE of Au-PSCs at 23.5%. Even without encapsulation, the devices demonstrate exceptional
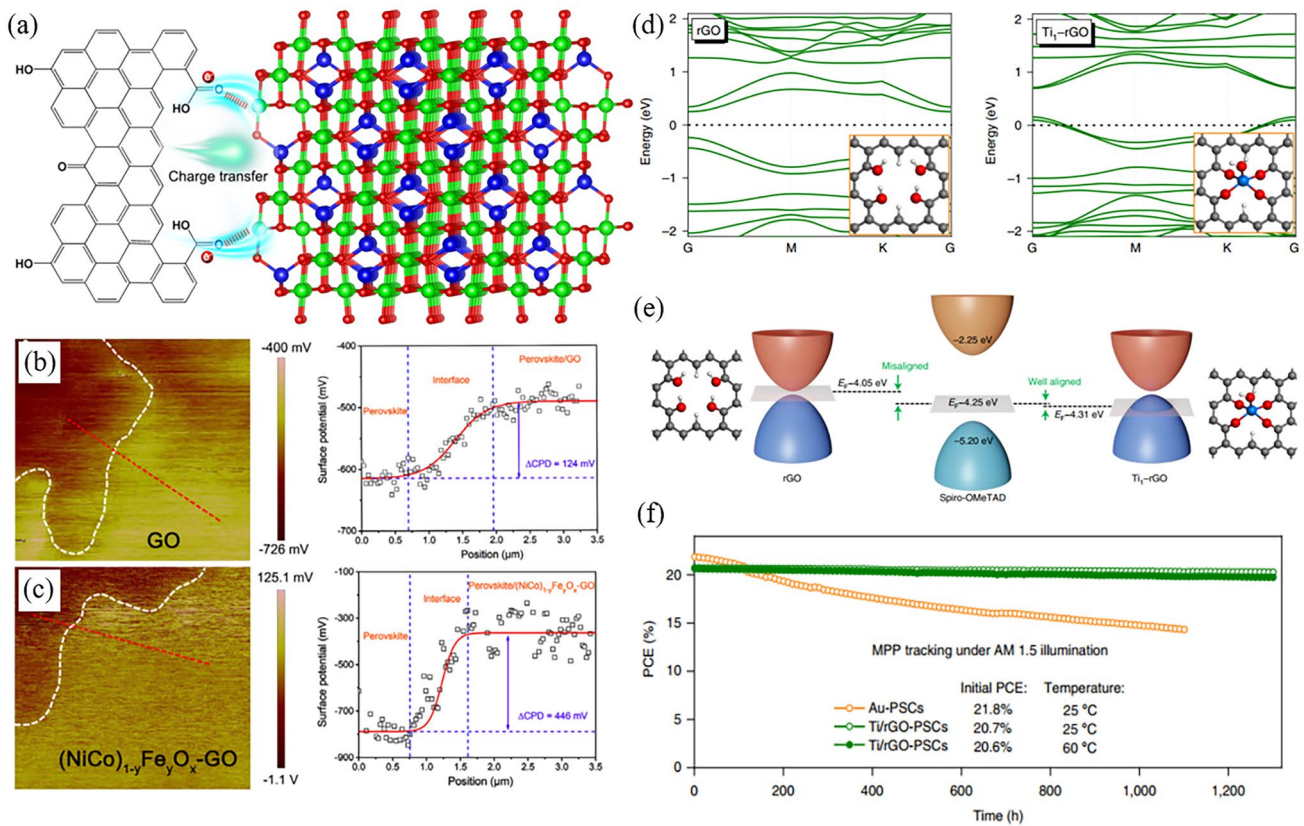
Fig. 8 a Schematic illustration of the transfer of charge from GO to inorganic NPs. **b, c** Surface potential patterns and corresponding surface contact potential difference values (obtained along the red lines) at the **b** GO/perovskite and **c** NP-GO/perovskite interface. Reproduced with permission from Ref. [177]. Copyright 2021, Wiley. **d** The energy band structure of rGO and Ti_1–rGO calculated by density functional theory. **e** Schematic band alignment of between spiro-OMeTAD and electrode materials (rGO and Ti_1–rGO). **f** Maximum power point aging of Ti_1–rGO-based C-PSC (25 and 60 °C, respectively) and conventional thermal evaporation Au–PSC (25 °C) under an N_2 atmosphere, one-sun continuous illumination. Reproduced with permission from Ref. [52]. Copyright 2021, Springer Nature

stability, with 98% and 95% retention of their initial values after 1,300 h of one-sun illumination at 25 and 60 °C, respectively (Fig. 8f).

4.2 Transitional Metal Dichalcogenides

As growth templates, TMDs have found widespread applications at the bottom interface, but reports on their utilization at the top interface are comparatively scarce. This disparity might be attributed to the distinct band structure and conductivity characteristics of these materials. MoS_2 stands out as a successful example among TMDs, with its combination of high hole mobility and the ability to form favorable heterojunctions with perovskites. Consequently, it is frequently mentioned as a promising HTL or ABL for PSCs. However, the WF of pristine MoS_2 is below 4.8 eV,

which is lower than that of most commonly used HTMs [178]. For example, spiro-OMeTAD has a higher WF of 4.9 eV, while the WF of PEDOT: PSS ranges from 5.0 to 5.2 eV [179–181]. This suggests that 2D MoS_2 may have insufficient capacity for hole extraction. In addition, the narrow optical bandgap (~ 1.2–1.8 eV) of 2D MoS_2 positions its CBM at ~ -4.3 eV, which is lower than the lowest occupied energy level of the $MAPbI_3$ (~ -4.0 eV) [182]. This characteristic hinders its effectiveness of electrons transport. In order to address this issue, a vdW hybridization architecture composed of zero-dimensional MoS_2 quantum dots (MoS_2 QDs) and rGO has been proposed [183]. These two materials are interacted through either the vdW physical adsorption of sulfur-sulfur (S–S) bonds or the S-vacancies passivation/filling (Fig. 9a). As a result of the quantum confinement effect, the optical bandgap and CBM of MoS_2 is increased

from 1.4 eV to over 3.2 eV and from -4.3 to -2.2 eV, respectively, which helps to reduce the backflow of electrons into the HTL (Fig. 9b). On the other hand, the rGO flakes plug the pinholes in the MoS_2 QDs films, ensuring complete coverage of the perovskite film by this hybridized HTL. The synergy of MoS_2 QDs and rGO has enhanced the J_{SC} (20.28 to 22.81 mA cm^{-2}) and V_{OC} (1.07 to 1.11 V) of the $MAPbI_3$ based PSCs, leading to an increase in the PCE from 16.85% to 20.12%. Similarly, the energy level of MoS_2 can also be regulated by linking thiol group of 3-mercaptopropionic acid (MPA) moieties on its surface [184]. As an ABL between perovskite and spiro-OMeTAD, this chemically functionalized MoS_2 (fMoS_2) exhibited high FF and J_{SC} for large-area PSMs. Consequently, the $fMoS_2$ decorated PSMs with active areas of 82 and 108 cm^2 achieved PCE of 15.3% and 13.4%, respectively. As a comparison, the PCE for their pristine MoS_2 counterparts is 13.56% and 12.5%, respectively. In a recent breakthrough, by modifying the bottom

and top interfaces with graphene and $fMoS_2$, respectively, the PCE of the perovskite module with aperture area of 101 cm^2 reached 16.4% [53]. Encouragingly, perovskite panels assembled with the modules reached a peak power exceeding 250 W under outdoor conditions (total area of 4.5 m^2). As a stand-alone solar farm infrastructure, these panels have been operating for 12 months and achieved a remarkable T_{80} of 5,832 h (Fig. 9c, d). These results indicate a significant advancement in the practical utilization of perovskite photovoltaic technology.

Besides, it has been discovered that MoS_2 serves as a complementary layer to the dopant-free HTL due to its fast vertical charge transport and robust chemical stability. For example, in regular PSCs with CsFAMA ternary cations, an ultrathin layer of MoS_2 is sandwiched between the perovskite and the dopant-free PTAA [165]. The VBM of MoS_2 is -5.4 eV, which shows an improved energy level alignment and reduces the barrier between PTAA (-5.1 eV) and
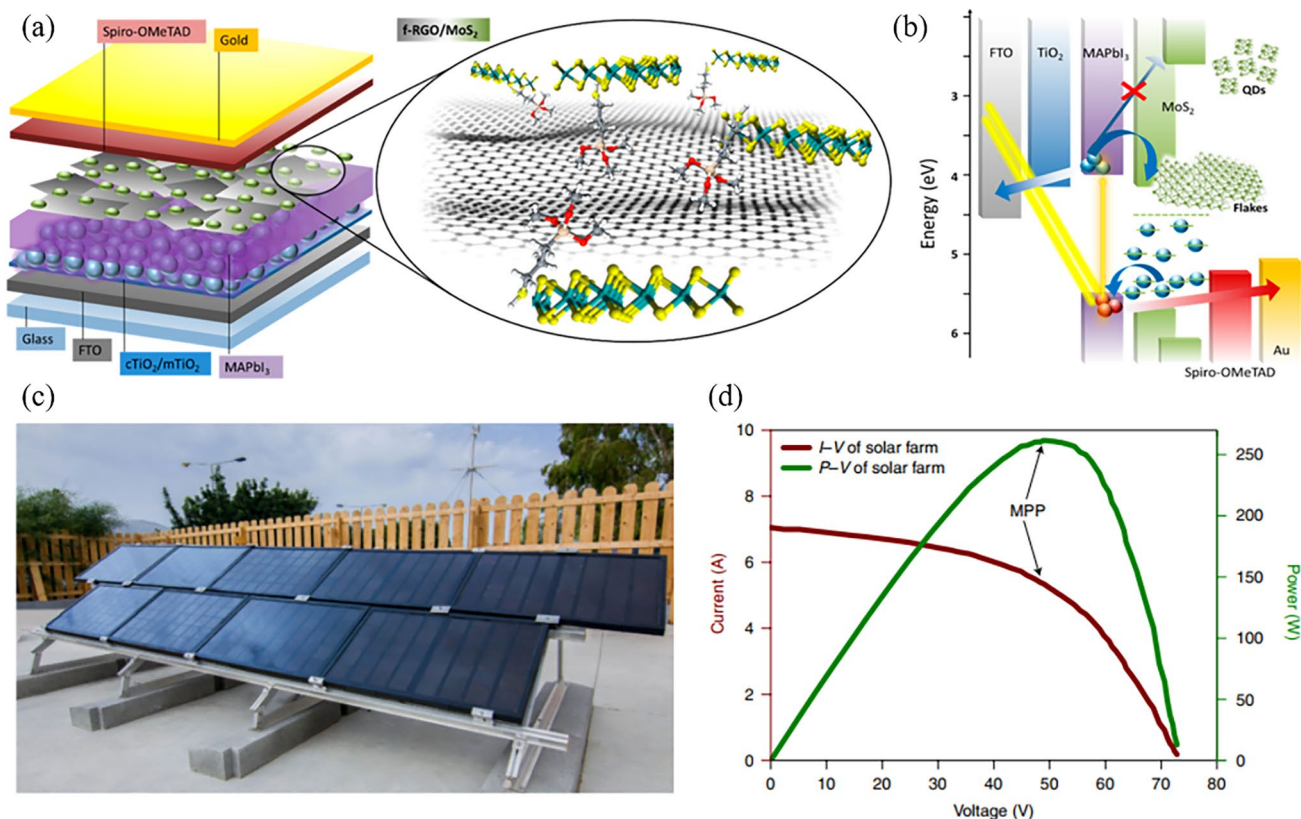

Fig. 9 **a** Schematic illustration and **b** energy level diagram of PSC modified with MoS_2 QDs:f-rGO hybrids. Reproduced with permission from Ref. [183]. Copyright 2018, American Chemical Society. **c, d** Integration of panels into a stand-alone solar farm. **c** Nine panels integrated in a stand-alone solar farm-powered infrastructure installed in Crete, HMU campus. **d** Typical *I–V* and *P−V* characteristics of the solar farm with a maximum output power (P_m) of ∼ 261 W_p. Reproduced with permission from Ref. [53]. Copyright 2022, Springer Nature

CsFAMA (− 5.65 eV). The serial resistance of the modified device decreased from 3.21 to 2.85 Ω cm^{-2}, while the shunt resistance increased from 3.85 to 7.09 kΩ cm^{-2}. These improvements in electrical contact have enhanced the V_{OC} (0.887 to 1.05 V) and FF (74.64% to 79.96%) of PSC, resulting in an increase in PCE from 15.04% to 18.54%. Due to the absence of doping in PTAA and the enhanced hydrophobicity of the interface provided by MoS$_2$, this device exhibits strong moisture resistance under ambient conditions. In addition, it has been demonstrated that the incorporation of MoS$_2$ into flexible PSCs can enhance both their mechanical and light stability. Through the surface modification of the perovskite with 1-dodecanethiol (DT) and MoS$_2$, the polyethylene terephthalate (PET)/ITO-based PSC exhibits complete recovery in terms of PCE, V_{OC}, J_{SC}, and FF after undergoing 300 cycles of bending tests [185]. Even after a conventional light exposure cycle, the unencapsulated device manages to retain an impressive 95% of its original PCE. In contrast, the control sample experiences a significant decline, dropping to only 32% of its original PCE under the same conditions.

4.3 MXenes

Given the ability to finely tune the WF of MXenes over a wide range during their synthesis (1.6 eV for OH terminations to 6.25 eV for O terminations), this characteristic enables facile control of the energy levels of perovskite and CTLs [186]. For instance, by co-doping the MAPbI$_3$ absorber layer and 1-(3-methoxycarbonyl)-propyl-1-phenyl-(6,6)-C$_{61}$ (PCBM) with Ti$_3$C$_2$T$_x$, it was observed that the WF of the two were adjusted by ~ 60 and ~ 200 meV, respectively [187]. This improvement facilitates the extraction and transport of photogenerated electrons across the top interface. In addition, the facile surface chemical modification of Ti$_3$C$_2$T$_x$ allows for straightforward adjustment of its optoelectronic properties. By incorporating Lewis acid CdCl$_2$ during the ultrasonic exfoliation of the Ti$_3$AlC$_2$, Ti$_3$C$_2$Cl$_x$ terminated with Cl- can been obtained. The as-prepared 2D nanosheets have advantages for use in all-inorganic CsPbBr$_3$ PSCs with a configuration of FTO/SnO$_2$-TiO$_x$Cl$_{4-2x}$/CsPbBr$_3$:Ti$_3$C$_2$Cl$_x$/Ti$_3$C$_2$Cl$_x$/carbon [188]. Due to the strong bonding energy of Cl atoms, the Pb^{2+}-Cl-Ti$_3$C$_2$ bridging connection at the top interface functions as a lattice "tape" that restrains the expansion of the perovskite. This

mechanism improves the crystalline quality of perovskite films and enhancing the thermal stability of the interfaces. As a result, the Ti$_3$C$_2$Cl$_x$-modified device demonstrates an enhancement in PCE from 9.18% (with V_{OC} = 1.569 V, J_{SC} = 7.32 mA cm^{-2}, FF = 79.9%) to 11.08% (with V_{OC} = 1.702 V, J_{SC} = 7.87 mA cm^{-2}, FF = 82.7%). These achievements place it at the forefront in the field of all-inorganic CsPbBr$_3$ PSCs. Similarly, introducing fluorine functionalized MXene QDs (Ti$_3$C$_2$F$_x$ QDs) as a passivation layer between the CsPbI$_3$ absorber layer and the sprio-OMeTAD HTL, the device exhibits an excellent PCE of 20.44% with a high V_{OC} of 1.22 V [189]. Moreover, in order to suppress the migration of iodide ions from the perovskite layer to the Ag cathode, tetrabutylammonium bromide-modified Ti$_3$C$_2$T$_x$ (TBAB-Ti$_3$C$_2$T$_x$) was developed as a cathode buffer layer (CBL) between PCBM and the Ag cathode [190]. The calculations by density functional theory indicate that partial of the charge in TBAB transfers to Ti$_3$C$_2$T$_x$ via the N and Br atom. This mechanism improves the conductivity of TBAB-Ti$_3$C$_2$T$_x$ and reduces its WF from 4.5 to 3.9 eV, which is more compatible with the energy level of MAPbI$_3$. The PCE of the TBAB-Ti$_3$C$_2$T$_x$-based device reached 21.65%, exceeding that of the device with BCP as the CBL (19.94%).

Despite the performance enhancement achieved in MXenes-based PSCs, the operational stability of the device is still not satisfactory. To address this issue, nano-MXenes with tailored halogen-terminated surfaces (F$_x$, Cl$_x$, Br$_x$, I$_x$) were prepared through pulsed laser irradiation [191]. Halogen anions have the ability to stabilize the soft perovskite lattice, thereby establishing a robust interface between MXenes and perovskite layers (Fig. 10c). This strategy regulates the deep-level defects and WF of the interface, as well as reducing the charge transport barrier. The champion device exhibits a high PCE of 24.17%, and it maintains a consistent performance of over 90% even after operating at the maximum power point for 1,000 h. In addition, it is observed that when Ti$_3$C$_2$T$_x$ is oxidized by NaOH aqueous solution, anatase TiO$_2$ nanoparticles can be formed on its surface [170]. The kelvin probe force microscopy results indicate that the oxidized Ti$_3$C$_2$T$_x$ strengthens the electric field at the perovskite/ETL interface and expands the depletion region throughout the perovskite layer (Fig. 10a, b). With such a surface engineering approach, the inverted CsPbI$_3$ PSC attains a PCE of 19.69% (0.096-cm^2) and 14.64% (25-cm^2 minimodules), respectively. After enduring more than 1,000 h of simultaneous exposure to damp heat (85 °C/85%

RH) and intense 1-sun light soaking, the encapsulated mini-module maintains 85% of its initial PCE. Recently, 3-phos-phonopropionic acid (H3pp) has been reported as an additive to obtain functionalized MXene Ti_3C_2 (MXene:H3pp), which further forms a HP/MXene:H3pp heterojunction with Halide Perovskite (HP). This strategy strengthens the connection between the perovskite layer, the interface, and the Mxene, resulting in an increase in device PCE from 20.56% to ~22% [192]. Encouragingly, after outdoor testing (ISOS-O) carried out for > 600 h, the MXene-modified device reveals a T_{80} of ~600 h, while the control device degrades completely (Fig. 10d). This is the first report of the stability assessment of MXene-based PSCs carried out under real outdoor conditions, which pave the way for the commercialization of PSCs.

4.4 Black Phosphorus and Other 2D Materials

The electronic band structure of BP is dependent on its number of layers due to its puckered orthorhombic lattice, quantum confinement effects, and interlayer interactions [43, 100]. This imparts a unique characteristic to the material for interface engineering. For instance, in order to enhance the performance of all-inorganic PSCs with a structure of FTO/c-TiO_2/$CsPbI_3$/CuSCN/Au, different layers of BP were spin-coated between the $CsPbI_3$ and the CuSCN HTL [193]. It is revealed that a BP layer count ranging from one to two exhibits a remarkable harmony in energy levels with $CsPbI_3$. Moreover, the dielectric shielding effect of BP leads to an improved dissociation efficiency of excitons, resulting in an increase in the carrier density of $CsPbI_3$ from 1.92×10^{14} to 2.82×10^{14} cm^{-3}. As a result, the PCE of the all-inorganic PSC enhanced from 10.48% (with $V_{OC} = 1.02$ V, $J_{SC} = 15.8$ mA cm^{-2}, FF = 65.1%) to 14.17% (with $V_{OC} = 1.08$ V, $J_{SC} = 19.3$ mA cm^{-2}, FF = 68.4%), which was considered as the state-of-the-art performance at that time. The recent studies indicate that BP, with its superior hole mobility (~ 1,000 cm^2 V^{-1} s^{-1}), allows for effective conduction of holes out of the perovskite grain boundaries [194]. This finding confirms that the presence of grain boundaries in perovskite does not have a detrimental effect on the performance device, as long as the accumulated charge carriers within it are promptly evacuated. On the contrary, the combination of grain boundaries and BP
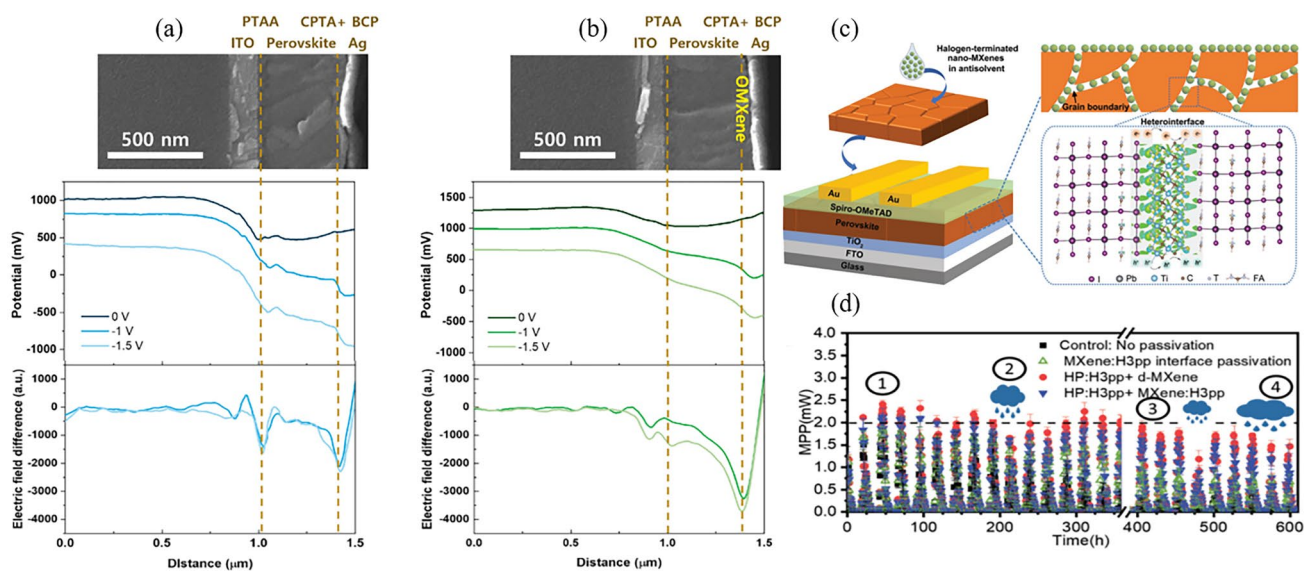

Fig. 10 **a, b** Kelvin probe force microscopy for electrical potential and field profiling on the cross-sectional surfaces of PSCs **a** without and **b** with OMXene. Reproduced with permission from Ref. [170]. Copyright 2022, Elsevier. **c** Schematic illustration of PSCs embedding of halogen-terminated nano-MXenes. The functional heterointerface between the perovskite and nano-MXenes is achieved via Pb-T-based ionic lattice anchoring. Reproduced with permission from Ref. [191]. Copyright 2022, Wiley. **d** ISOS-O protocol tracking for PSCs employing bulk and interface passivation. obtained averaged maximum power point values for 3–4 devices for each category during 600 h by holding the encapsulated devices at their open-circuit voltage and recording their *J-V* by 20-min intervals in outdoor at Barcelona, 41.5021°N, 2.1039°E, Spain. Reproduced with permission from Ref. [192]. Copyright 2023, Wiley

creates a fast path for hole transport, resulting in higher hole current density (Fig. 11a, b).

In spite of the impressive performance of BP, the prevailing approach for preparing BP relies on liquid-phase exfoliation assisted by ultrasonic treatment. Unfortunately, this method inevitably introduces impurities and defects that compromise the electronic characteristics of BP. Moreover, the inadequate lateral size of BP can lead to an uneven distribution within interfaces, limiting its full utilization and potential advantages. To effectively tackle these challenges, an innovative synthetic technique through electrochemical delamination has been proposed (Fig. 11c) [168]. This method allows for the achievement of average lateral dimensions of both BP and fluorinated BP (F-BP) at a remarkable magnitude of 4.75 μm, with a thickness spanning only 4–5 atomic layers (Fig. 11d, e). When used as interlayers for hole injection between the perovskite and spiro-OMeTAD, these large-scale, high-quality BP and F-BP nanosheets demonstrate outstanding performance, as the PCE of the device has been enhanced from the initial value of 19.63% (control) to 20.76% (BP) and 22.06% (F-BP), respectively. It is noteworthy that

F-BP demonstrates superior stability in comparison to BP. This can be attributed to the formation of hydrogen bonds with MA^+ and FA^+ ions, as well as ionic bonding with Pb^{2+} ions, which is facilitated by the presence of F^-. Additionally, the modification with fluorine enhances the inherent antioxidant and moisture resistance properties of BP.

In addition, antimonene, CNs, MOFs, and 2D perovskite materials have also been reported to be used for the top interface of PSCs [69, 70, 195, 196]. Among them, 2D perovskite materials are particularly noteworthy. Despite exhibiting impressive PCE as a light-absorbing material in photovoltaic devices, the stability of 3D perovskite has remained a persistent challenge [197, 198]. On one hand, the weak hydrogen or ionic bonding between small A cations and corner-sharing BX_6 octahedra renders 3D perovskite compounds vulnerable upon exposure to moisture or polar solvents. This leads to irreversible decomposition, compromising their stability and lifetime. On the other hand, the fabrication of 3D polycrystalline films through solution processing inevitably gives rise to various inherent defects on their surface. Furthermore, during the crystallization process, intense visible pinholes
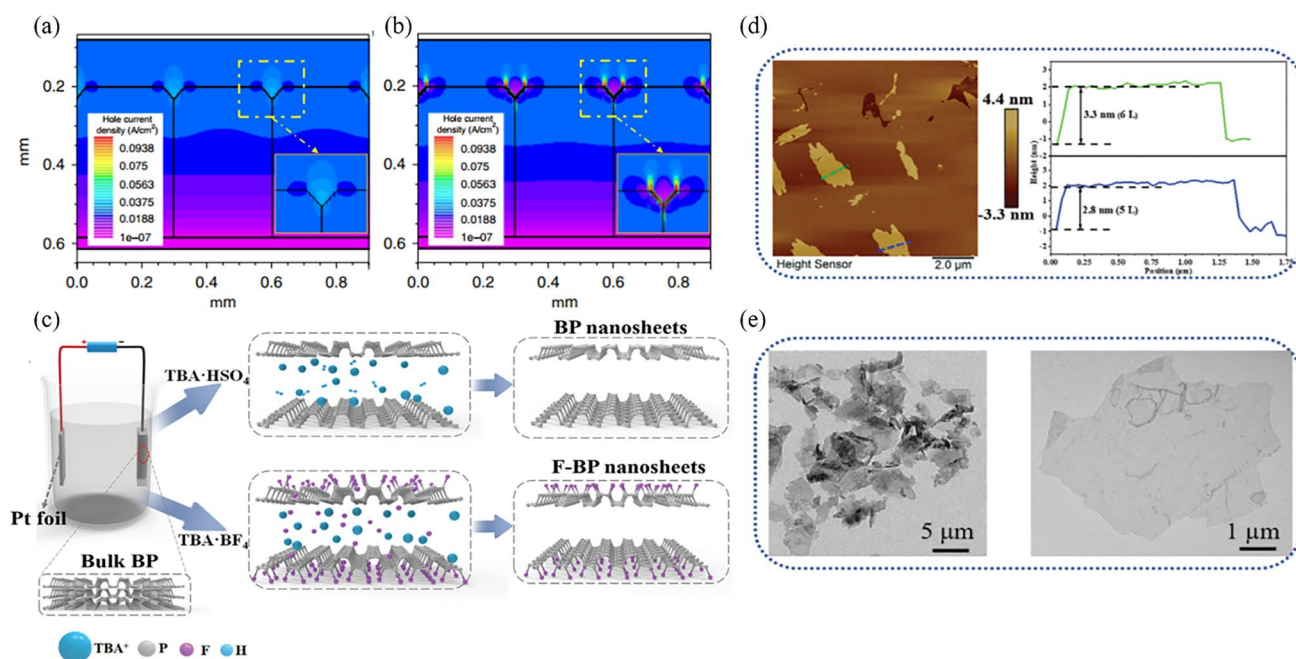

Fig. 11 a, b The simulated hole current density distribution for the PSCs **a** without and **b** with BP modification. Reproduced with permission from Ref. [194]. Copyright 2021, AAAS. **c** Schematic illustration of the delamination procedure in a two-electrode reaction cell. **d** Atomic force microscope and **e** Transmission electron microscopy images of F-BP nanosheets. Reproduced with permission from Ref. [168]. Copyright 2022, Wiley

and cracks commonly emerge. These unavoidable imperfections induce severe charge recombination, resulting in considerable energy loss [32, 35].

In order to deal with these problems, 2D perovskite materials with improved stability and elevated activation energy have garnered significant interest [13, 162, 199]. Unlike their fragile 3D counterparts, 2D perovskites consist of larger amine cations, such as butylamine (BA) and phenethylamine (PEA), which are coordinated within the cages of inorganic BX_6 octahedra. Due to the large radius of the organic amine cation, the upper and lower inorganic slabs cannot be linked by shared corners, leading to the formation of a 2D structure with alternating organic and inorganic layers [200, 201]. The crystal structure of 2D perovskites can be envisioned as the cleaving of the 3D network of ABX_3 perovskite along the (100), (110), and (111) planes, resulting in the formation of (100), (110), and (111)-oriented 2D perovskites, respectively [30, 115]. Among these orientations, the (100) has been demonstrated to be the most favorable structure for solar cells. Based on the number of coordinative amino heads present in the spacer cations, this subgroup can be further categorized into three distinct phases: the Ruddlesden–Popper (RP) phase, the Dion–Jacobson (DJ) phase, and the alternating cations in the interlayer space (ACI) phase. Notably, 2D perovskite can be used as a light-absorbing material to constitute photovoltaic devices. Nevertheless, its narrower absorption spectrum and inferior carrier transport efficiency render devices utilizing 2D perovskite less efficient compared to those based on 3D perovskite [202, 203].

By harnessing the complementary advantages of both 3D and 2D perovskites, researchers crafted 2D/3D perovskite heterostructures to achieve the coexistence of high efficiency and ultrastability in PSCs [204–206]. There are primarily two methods for fabricating this stacking-layered architecture: one involves mixing a 2D precursor material with a 3D precursor solution, while the other involves forming a 2D/3D bilayer structure through the reaction of a 2D precursor solution on the surface of a 3D layer. Overall, the combination of 3D and 2D perovskites is achieved through chemical bonding, facilitated by the presence of a pair of non-bonding electrons originating from the N in amines. The merits of 2D/3D heterostructures are as follows [30, 201]: (i) The lattice discrepancies between 2 and 3D perovskites induce surface reconstruction of the 3D material, effectively reducing defects at its grain boundaries and surfaces. Additionally, the sizeable organic iodonium salt simultaneously fills cation/anion vacancies, interacts with under-coordinated lead clusters, and embeds into surface boundaries, pinholes, and cracks. (ii) Compared to 3D perovskites with small A cations, the strengthened molecular interaction between bulky organic cations and inorganic octahedral units contributes to superior photo- and thermal stability. Moreover, the hydrophobic nature of bulky organic cations, coupled with the formation of atomically dense layers, provides a steric hindrance that prevents erosion caused by humidity/oxygen and suppresses ion migration. (iii) 2 and 3D perovskites possess high and low energy levels, respectively. The distinct energy level difference in 2D/3D heterostructures can facilitate carrier extraction and transport.

Currently, remarkable advancements in the performance of PSCs have been realized through the utilization of 2D/3D stacked heterojunctions [196, 207]. For example, the researchers spin-coated pre-synthesized 2D perovskite ($(BA)_4AgBiBr_8$) nanosheets onto the surface of 3D-$FAPbI_3$-based perovskite [71]. Due to the vdW force and the large bandgap of $(BA)_4AgBiBr_8$ (2.35 eV), a type-I heterojunction was obtained. This novel contact creates a barrier at the top interface, which inhibits trap-assisted recombination and mitigates the iodide ion diffusion from perovskite to the metal electrode. As a result, a satisfying PCE of 24.48% is achieved with an improved V_{OC} from 1.13 to 1.17 V. After continuous irradiation for 1,000 h, the 3D/2D established PSCs retain ~ 90% of their initial PCE. However, the solution-based preparation of 2D perovskites lacks control over phase purity, film thickness, and orientation, which poses challenges for efficient carrier extraction and transport between 3 and 2D perovskites. Therefore, solvent-free preparation techniques have been proposed as a viable strategy. For instance, Noh et al. developed a solid-state in-plane growth (SIG) approach, which facilitates the growth of pure-phase and thickness-tunable BA_2PbI_4 films on FA-based 3D perovskite films [208]. The intact 2D/3D halide junction, upon formation, not only extends the carrier lifetime but also establishes an ideal back-surface field for efficient hole transfer. The PSCs with the intact 2D/3D junction demonstrate a remarkably enhanced PCE of 24.59%. Furthermore, these devices maintain an impressive 94% of their initial PCE even after enduring a 1,056-h damp heat test (85 °C/85% RH).

5 Graphene Electrodes

The ideal electrode material should possess a commendable level of electrical conductivity, a WF that harmonizes with the neighboring CTLs, exceptional chemical and mechanical stability, all while being cost-effective [22]. Furthermore, for the transparent electrode and back electrode, it is requisite that they exhibit abundant transparency and reflectivity, respectively. Traditional electrode materials utilized in PSCs, including FTO, ITO, Ag, and Au, often suffer from inadequate mechanical and chemical stability, as well as relatively high prices [36, 38]. To address these challenges, 2D graphene has garnered increasing attention in recent years due to its excellent electrical conductivity, high transmittance, large surface area, and stable mechanical properties [37, 60, 209].

5.1 Graphene as Transparent Electrodes

The enthusiasm for exploring 2D graphene as a transparent electrode primarily stems from the necessity in fabricating flexible solar cells. These types of cells find extensive application in powering energy supply systems for wearable electronic devices, the Internet of Things, intelligent communication, portable electronic products, etc. [37, 210–212]. The customary preference for ITO/polyethylene naphthalate (PEN) as the substrate for the fabrication of flexible PSCs is well-documented. Nonetheless, the scarcity of indium, a rare resource, poses challenges for the long-term sustainability and advancement of the photovoltaic industry. In addition, it should be noted that the use of ITO in solar cells is often accompanied by issues such as mechanical instability. According to reports, solar cells using ITO/PEN substrate with an initial PCE of 12.2% could only maintain 50% after undergoing 1,000 bends at a bending radius of 4 mm [213]. In contrast, 2D graphene exhibits exemplary optical and electrical attributes, while maintaining mechanical stability and strong chemical inertness. Furthermore, owing to the abundant reserves of carbon, it emerges as the ideal alternative for fabricating flexible and transparent electrodes.

Doping plays a crucial role in regulating the WF and series resistance, as well as carrier collection efficiency of graphene electrode. In the past, researchers often adopted $AuCl_3$ as a doping agent for graphene [216]. However, the inherent absorption of $AuCl_3$ results in certain optical losses, which indicates an urgent need to explore novel dopant. Recently, bis(trifluoromethanesulfonyl)-amide[$((CF_3SO_2)_2NH)$] (TFSA) has been found to be an effective dopant in graphene [217]. The researchers have uncovered the significance of doping concentration in influencing the optoelectronic characteristics of graphene. It was found that by attaining a concentration of 20 mM in TFSA, the graphene exhibited substantial improvements in both sheet resistance and WF. The original values of these two parameters, 650 for sheet resistance and -4.52 eV for WF, have been adjusted to 116 and -4.90 eV, respectively. On the other hand, there is only a slight decrease in transmittance, with the value shifting from 97.18% to 96.80%. In addition, the incorporation of lithium bis(trifluoromethane) sulfonimide (Li-TFSI) as a dopant has been highlighted for both a single-layer graphene substrate and its neighboring PTAA HTL (Fig. 12a) [214]. Through this modification, a PCE of 19.01% was achieved for a flexible device with an active area of 1 cm^2 (Fig. 12b), which represents the highest reported PCE among flexible, TCO-free PSCs. Moreover, this type of device demonstrates excellent bending and light stability. After continuous illumination for 1,000 h, the PCE remained at a remarkable 80%.

The versatility of carbon bonds enables carbon materials to function as both p-type and n-type semiconductors, while also exhibiting properties similar to metals [37]. Consequently, there has been a growing interest in the development of all-carbon electrodes, HTL-free, and flexible PSCs. This innovative approach not only presents an alternative opportunity to address the cost and stability concerns associated with photovoltaic technology, but also holds promise for future breakthroughs. For example, a PCE of 8.4% has been achieved in a device with architecture of PET/Graphene/TiO_2/PCBM/$MAPbI_3$/cross-stacking carbon nanotubes (Fig. 12c) [212]. This all-carbon electrode-based, HTL-free PSC presents extraordinary mechanical stability in comparison to ITO-based counterparts. Moreover, it outperforms devices using Au and Ag electrodes in terms of both light soaking and thermal stress resistance. Further investigations have shown that replacing the TiO_2 ETL with vapor-deposited C_{60} produces a notable reduction in the notorious hysteresis, concurrently achieving a PCE of 13.93% [60].

Despite the remarkable performance exhibited by graphene electrodes, it is important to note that the synthesis of graphene on a large scale requires high temperatures reaching up to 1000 °C [38]. Additionally, when
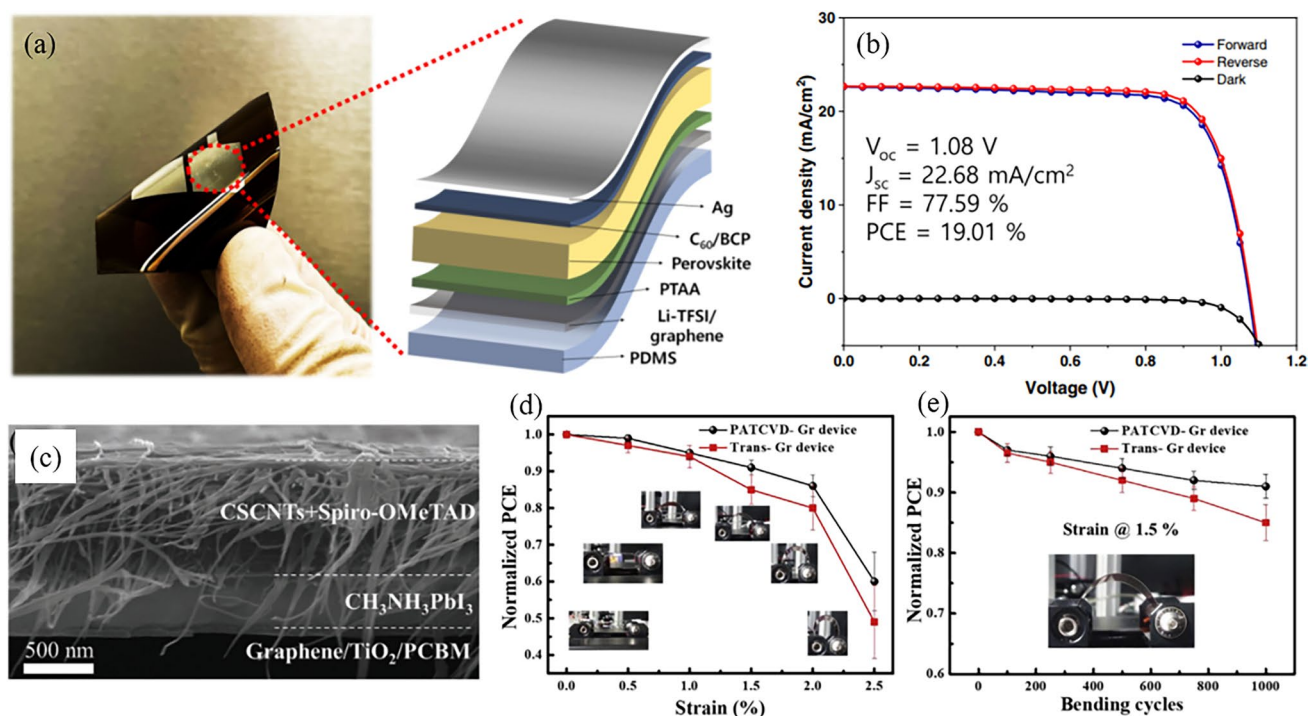
Fig. 12 a Photograph and schematic illustration of the Li-TFSI-treated graphene/PTAA transparent electrode-based PSCs with an active area of 1 cm² and **b** corresponding J–V curves. Reproduced with permission from Ref. [214]. Copyright 2021, Wiley. **c** Cross-sectional scanning electron microscopic image of the all-carbon-electrode-based flexible PSCs. Reproduced with permission from Ref. [212]. Copyright 2018, Wiley. **d, e** Variations in the normalized PCEs **d** measured after 1,000 bending cycles at each tensile strain and **e** as a function of bending cycle under a tensile strain of 1.5%. Reproduced with permission from Ref. [215]. Copyright 2019, Elsevier

attempting to fabricate flexible PSCs, the transfer of graphene from alternative substrates onto a polymer base can lead to structural nonuniformities in the final samples, including wrinkles, ripples, and lattice defects [218]. These factors impose limitations on the commercialization of graphene electrodes and also have an impact on the fabrication of high-quality PSCs. To address these issues, several novel techniques characterized by low-temperature, non-transferability have been proposed. For instance, the researchers have successfully achieved the direct fabrication of monolayer graphene on flexible polyestersulfone substrates using plasma-assisted thermal chemical vapor deposition (PATCVD) [215]. Notably, this technique necessitates a mere temperature of 150 °C for thin film growth. Following this groundwork, PSCs with a 300 nm-thick perovskite absorber layer have been prepared and yields a PCE of ~ 14.2%. Significantly, even after undergoing 1,000 cycles of bending, these devices maintain a retention rate of 90% of their initial PCE (Fig. 12d, e). Moreover, the interface contact between graphene and

adjacent semiconductors can be improved through surface functionalization. As an example, recent findings have shown that surface engineering with ethylene glycol enhances the abundance of surface active sites on graphene, thereby facilitating the deposition of ZnO thin films through atomic layer deposition [219]. This approach reduces interfacial resistance, enhances photon transmission, and consequently results in improved efficiency and stability of the PSCs.

5.2 Graphene as Back Electrodes

There are two key factors driving the research on the utilization of 2D graphene as back electrodes in PSCs: (1) Traditional carbon electrode materials have a porous structure that is characterized by numerous gaps and grain boundaries. These features hinder their ability to establish close contact with the charge transport layers or the perovskite films [220, 221]. (2) With the emergence of semi-transparent

solar cells, there is a growing need for back electrodes that combine high conductivity with transparency [222, 223]. Among various options, 2D graphene stands out as an ideal material that satisfies these requirements.

To enhance the interface contact between graphene and perovskite, nitrogen-doped graphene frameworks (N-GFs) have been synthesized via a facile one-step fast pyrolysis [224]. The as-prepared composite material exhibits a large specific surface area (1149 m^2 g^{-1}), which enables a full-cover adsorption with the perovskite layer. These properties make it capable of replacing expensive organic HTL and noble metal electrodes, serving as the top electrode in HTL-free PSCs. Moreover, the introduction of nitrogen atoms provides additional lone pair electrons, which results in localized strain within the hexagonal carbon lattice. Compared to the undoped graphene, N-GFs have improved the J_{SC} (18.69 to 20.02 mA cm^{-2}) and FF (55.89% to 59.25%) of the HTL-free PSC (FTO/TiO$_2$/MAPbI$_3$/graphene), resulting in an increase in the PCE from 8.98% to 10.32%. In a recent study, it has been unveiled that the co-doping of graphene with Ni and N (Ni-NG) can decrease the WF of graphene (5.29 to 5.02 eV), thereby enhancing the injection dynamics of holes [225]. Additionally, the presence of Ni atoms on the graphene surface provides an abundance of active sites, which leads to a more intimate interface contact that facilitates the extraction and transport of charge carriers. After implementing this modification, the PCE of PSC with architecture of FTO/SnO$_2$/perovskite/Ni-NG/carbon has achieved a noteworthy 12.39%.

In order to establish a favorable electrical contact between the carbon electrode and the CTL to minimize sheet resistance and facilitate the large-scale fabrication of the PSCs, an innovative modular approach has been demonstrated. In this scenario, the main body of the solar cell and the carbon top electrode are prepared separately, and subsequently assembled by applying a specific level of pressure (Fig. 13) [220]. The sheet resistance is directly influenced by the magnitude of applied pressure. When the optimal pressure is applied, these two factors create a strong Ohmic contact with minimal series resistance. The authors conducted a comparative analysis of the performance of three carbon electrodes: carbon black, graphite sheet, and 2D graphene. Among them, 2D graphene exhibited the most outstanding overall performance, with a PCE reaching an impressive 18.65%. This achievement stands as one of the highest reported PCE for carbon electrodes in PSCs. Similarly, the researchers first created a hybrid graphene/carbon nanotube (CNT) film using transfer and wet etching techniques [221]. Afterward, they successfully transferred this hybrid film onto the HTL using a lamination process that does not involve water or chemical reactions. In addition to the reduction of resistance, it served as an impermeable shield, safeguarding the interior of the PSCs against the corrosive erosions inflicted by ambient humidity.
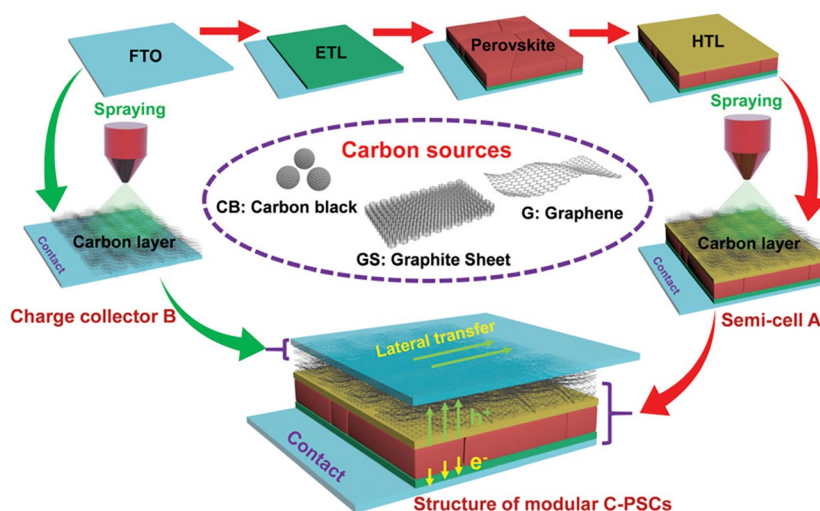

Fig. 13 Overview of the fabrication process for the modular C-PSCs; the insets display the microstructure diagrams of the three carbon source materials (CB, GS, and G). Reproduced with permission from Ref. [220]. Copyright 2019, The Royal Society of Chemistry

6 Conclusion and Outlook

In summary, the recent progress of 2D materials in PSCs has been summarized, including graphene and its derivatives, TMDs, MXenes, BP, and others. Due to their unique structures and excellent properties, 2D materials have demonstrated remarkable significance in facilitating the vdW epitaxial growth of perovskites, enhancing charge dynamics, suppressing ion-, moisture-, and oxygen-induced degradation, and serving as electrodes.

Benefiting from these improvements, 2D materials-incorporated PSCs went through rapid advance toward uniting the high efficiency with stability. Notably, a graphene-based PSCs with initial PCE of 24.34% exhibited 5000 h operational stability at the maximum power point under continuous 1-sun illumination and passed the 85 °C/85% RH stability test [36]. In addition, perovskite panels, with total area of 4.5 m^2 and enhanced by graphene and fMoS$_2$, reached a peak power exceeding 250 W under outdoor conditions. As a stand-alone solar farm infrastructure, these panels have been operating for 12 months and achieved a remarkable T_{80} of 5,832 h [53]. These achievements suggest that the commercialization of PSCs is on the horizon. However, numerous challenges remain to be overcome to bridge the gap between laboratory prototypes and industrialization. The following suggestions are proposed to further accelerate the research of 2D materials in PSCs:

(1) Much more efforts are still imperative to deeply understand the underlying physics mechanism of the vdW heterojunction. Due to the distinct bonding characteristics, the growth of perovskite on 2D materials and the resulting interfacial contacts differ significantly from those on conventional substrates. Although vdW epitaxial growth has demonstrated its efficacy in enhancing the grain quality and orientation of perovskite, there remains limited understanding regarding the growth mechanism and the quantitative relationship between the perovskite film and the morphology, size, and thickness of the underlying 2D materials. The theoretical framework is essential to comprehend the nucleation and crystallization processes of perovskite films on 2D materials, as well as the transport mechanism of photogenerated carriers across this heterojunction. The in situ morphological and spectroscopic characterization techniques, such as the integrated differential phase contrast scanning transmission electron microscopy and in situ grazing-incidence X-ray diffraction measurements, may play a pivotal role in elucidating these intricate phenomena [10, 226].

(2) The uneven distribution and incomplete coverage of 2D materials at the interface is a great challenge. At present, 2D nanosheets are primarily produced through liquid-phase exfoliation, resulting in the formation of 2D nanosheets with considerable randomness in terms of thickness and shape, and their lateral dimensions are usually restricted to a narrow range of tens to hundreds of nanometers. Hence, it becomes essential to explore fabrication methods that allow for precise control over the morphology and layer number of 2D materials, while simultaneously yielding sizable lateral dimensions and minimized imperfections. In this regard, techniques such as electrochemical deposition and physical vapor deposition present promising avenues to fulfill these aspirations [100, 168].

(3) The utilization of 2D materials as electrodes still requires further exploration. The excellent electrical conductivity, mechanical strength, and large surface area of graphene make it an ideal candidate for the transparent and back electrodes. However, several issues must be addressed prior to its commercialization, including the agglomeration, high contact resistance, and the trade-off between high transparency and low sheet resistance. The integration of graphene with metal nanowires or CNTs in the form of a hybrid electrode holds great promise as a future direction. In addition, further exploration should be conducted on other 2D materials that possess the potential to serve as electrodes, such as 2D Ti$_3$C$_2$ [227–229].

Declarations

Conflict of Interest The authors declare no interest conflict. They have no known competing financial interests or personal relationships that could have appeared to influence the work reported in this paper. Liyuan Han is an editorial board member for Nano-Micro Letters and was not involved in the editorial review or the decision to publish this article.

References

1. A. Kojima, K. Teshima, Y. Shirai, T. Miyasaka, Organometal halide perovskites as visible-light sensitizers for photovoltaic cells. J. Am. Chem. Soc. **131**, 6050–6051 (2009). https://doi.org/10.1021/ja809598r

2. J. Burschka, N. Pellet, S.-J. Moon, R. Humphry-Baker, P. Gao et al., Sequential deposition as a route to high-performance perovskite-sensitized solar cells. Nature **499**, 316–319 (2013). https://doi.org/10.1038/nature12340

3. H. Chen, F. Ye, W. Tang, J. He, M. Yin et al., A solvent- and vacuum-free route to large-area perovskite films for efficient solar modules. Nature **550**, 92–95 (2017). https://doi.org/10.1038/nature23877

4. M. Liu, M.B. Johnston, H.J. Snaith, Efficient planar heterojunction perovskite solar cells by vapour deposition. Nature **501**, 395–398 (2013). https://doi.org/10.1038/nature12509

5. J. Park, J. Kim, H.-S. Yun, M.J. Paik, E. Noh et al., Controlled growth of perovskite layers with volatile alkylammonium chlorides. Nature **616**, 724–730 (2023). https://doi.org/10.1038/s41586-023-05825-y

6. S. Zhang, F. Ye, X. Wang, R. Chen, H. Zhang et al., Minimizing buried interfacial defects for efficient inverted perovskite solar cells. Science **380**, 404–409 (2023). https://doi.org/10.1126/science.adg3755

7. H. Tang, Z. Shen, Y. Shen, G. Yan, Y. Wang et al., Reinforcing self-assembly of hole transport molecules for stable inverted perovskite solar cells. Science **383**, 1236–1240 (2024). https://doi.org/10.1126/science.adj9602

8. R. Azmi, D.S. Utomo, B. Vishal, S. Zhumagali, P. Dally et al., Double-side 2D/3D heterojunctions for inverted perovskite solar cells. Nature **628**, 93–98 (2024). https://doi.org/10.1038/s41586-024-07189-3

9. R. Lin, J. Xu, M. Wei, Y. Wang, Z. Qin et al., All-perovskite tandem solar cells with improved grain surface passivation. Nature **603**, 73–78 (2022). https://doi.org/10.1038/s41586-021-04372-8

10. P. Shi, Y. Ding, B. Ding, Q. Xing, T. Kodalle et al., Oriented nucleation in formamidinium perovskite for photovoltaics. Nature **620**, 323–327 (2023). https://doi.org/10.1038/s41586-023-06208-z

11. R. Chen, S. Liu, X. Xu, F. Ren, J. Zhou et al., Robust hole transport material with interface anchors enhances the efficiency and stability of inverted formamidinium–cesium perovskite solar cells with a certified efficiency of 22.3%. Energy Environ. Sci. **15**, 2567–2580 (2022). https://doi.org/10.1039/D2EE00433J

12. C. Fei, N. Li, M. Wang, X. Wang, H. Gu et al., Lead-chelating hole-transport layers for efficient and stable perovskite minimodules. Science **380**, 823–829 (2023). https://doi.org/10.1126/science.ade9463

13. Q. Jiang, Y. Zhao, X. Zhang, X. Yang, Y. Chen et al., Surface passivation of perovskite film for efficient solar cells. Nat. Photonics **13**, 460–466 (2019). https://doi.org/10.1038/s41566-019-0398-2

14. Q. Jiang, J. Tong, Y. Xian, R.A. Kerner, S.P. Dunfield et al., Surface reaction for efficient and stable inverted perovskite solar cells. Nature **611**, 278–283 (2022). https://doi.org/10.1038/s41586-022-05268-x

15. Z. Li, B. Li, X. Wu, S.A. Sheppard, S. Zhang et al., Organometallic-functionalized interfaces for highly efficient inverted perovskite solar cells. Science **376**, 416–420 (2022). https://doi.org/10.1126/science.abm8566

16. M.A. Green, E.D. Dunlop, M. Yoshita, N. Kopidakis, K. Bothe et al., Solar cell efficiency tables (version 62). Prog. Photovolt. Res. Appl. **31**, 651–663 (2023). https://doi.org/10.1002/pip.3726

17. T. Wu, Z. Qin, Y. Wang, Y. Wu, W. Chen et al., The main progress of perovskite solar cells in 2020–2021. Nano-Micro Lett. **13**, 152 (2021). https://doi.org/10.1007/s40820-021-00672-w

18. <best-research-cell-efficiencies.Pdf>. https://www.nrel.gov/pv/assets/pdfs/best-research-cell-efficiencies.pdf

19. W. Peng, K. Mao, F. Cai, H. Meng, Z. Zhu et al., Reducing nonradiative recombination in perovskite solar cells with a porous insulator contact. Science **379**, 683–690 (2023). https://doi.org/10.1126/science.ade3126

20. J.Y. Kim, J.-W. Lee, H.S. Jung, H. Shin, N.-G. Park, High-efficiency perovskite solar cells. Chem. Rev. **120**, 7867–7918 (2020). https://doi.org/10.1021/acs.chemrev.0c00107

21. H. Zhang, L. Pfeifer, S.M. Zakeeruddin, J. Chu, M. Grätzel, Tailoring passivators for highly efficient and stable perovskite solar cells. Nat. Rev. Chem. **7**, 632–652 (2023). https://doi.org/10.1038/s41570-023-00510-0

22. J. O'Sullivan, M. Wright, X. Niu, P. Miller, P.R. Wilshaw et al., Towards a graphene transparent conducting electrode for perovskite/silicon tandem solar cells. Prog. Photovolt. Res. Appl. **31**, 1478–1492 (2023). https://doi.org/10.1002/pip.3739

23. P.K. Nayak, S. Mahesh, H.J. Snaith, D. Cahen, Photovoltaic solar cell technologies: analysing the state of the art. Nat. Rev. Mater. **4**, 269–285 (2019). https://doi.org/10.1038/s41578-019-0097-0

24. X. Lin, D. Cui, X. Luo, C. Zhang, Q. Han et al., Efficiency progress of inverted perovskite solar cells. Energy Environ. Sci. **13**, 3823–3847 (2020). https://doi.org/10.1039/d0ee02017f

25. Y. Li, H. Xie, E.L. Lim, A. Hagfeldt, D. Bi, Recent progress of critical interface engineering for highly efficient and stable perovskite solar cells. Adv. Energy Mater. **12**, 2102730 (2022). https://doi.org/10.1002/aenm.202102730

26. J. Xia, M. Sohail, M.K. Nazeeruddin, Efficient and stable perovskite solar cells by tailoring of interfaces. Adv. Mater. **35**, 2211324 (2023). https://doi.org/10.1002/adma.202211324

27. P. Yan, D. Yang, H. Wang, S. Yang, Z. Ge, Recent advances in dopant-free organic hole-transporting materials for efficient, stable and low-cost perovskite solar cells. Energy Environ. Sci. **15**, 3630–3669 (2022). https://doi.org/10.1039/d2ee01256a

28. Z. Saki, M.M. Byranvand, N. Taghavinia, M. Kedia, M. Saliba, Solution-processed perovskite thin-films: the journey from lab- to large-scale solar cells. Energy Environ. Sci. **14**, 5690–5722 (2021). https://doi.org/10.1039/d1ee02018h

29. Y. Yao, C. Cheng, C. Zhang, H. Hu, K. Wang et al., Organic hole-transport layers for efficient, stable, and scalable inverted perovskite solar cells. Adv. Mater. **34**, e2203794 (2022). https://doi.org/10.1002/adma.202203794

30. G. Wu, R. Liang, M. Ge, G. Sun, Y. Zhang et al., Surface passivation using 2D perovskites toward efficient and stable perovskite solar cells. Adv. Mater. **34**, e2105635 (2022). https://doi.org/10.1002/adma.202105635

31. F.H. Isikgor, S. Zhumagali, L.V.T. Merino, M. De Bastiani, I. McCulloch et al., Molecular engineering of contact interfaces for high-performance perovskite solar cells. Nat. Rev. Mater. **8**, 89–108 (2023). https://doi.org/10.1038/s41578-022-00503-3

32. H. Zhu, S. Teale, M.N. Lintangpradipto, S. Mahesh, B. Chen et al., Long-term operating stability in perovskite photovoltaics. Nat. Rev. Mater. **8**, 569–586 (2023). https://doi.org/10.1038/s41578-023-00582-w

33. S. You, H. Zeng, Y. Liu, B. Han, M. Li et al., Radical polymeric p-doping and grain modulation for stable, efficient perovskite solar modules. Science **379**, 288–294 (2023). https://doi.org/10.1126/science.add8786

34. C. Li, X. Wang, E. Bi, F. Jiang, S.M. Park et al., Rational design of Lewis base molecules for stable and efficient inverted perovskite solar cells. Science **379**, 690–694 (2023). https://doi.org/10.1126/science.ade3970

35. G. Nazir, S.Y. Lee, J.H. Lee, A. Rehman, J.K. Lee et al., Stabilization of perovskite solar cells: recent developments and future perspectives. Adv. Mater. **34**, e2204380 (2022). https://doi.org/10.1002/adma.202204380

36. X. Lin, H. Su, S. He, Y. Song, Y. Wang et al., *In situ* growth of graphene on both sides of a Cu–Ni alloy electrode for perovskite solar cells with improved stability. Nat. Energy **7**, 520–527 (2022). https://doi.org/10.1038/s41560-022-01038-1

37. Y. Xu, Z. Lin, W. Wei, Y. Hao, S. Liu et al., Recent progress of electrode materials for flexible perovskite solar cells. Nano-Micro Lett. **14**, 117 (2022). https://doi.org/10.1007/s40820-022-00859-9

38. H. Su, T. Wu, D. Cui, X. Lin, X. Luo et al., The application of graphene derivatives in perovskite solar cells. Small

Meth. **4**, 2000507 (2020). https://doi.org/10.1002/smtd.202000507

39. P. Miró, M. Audiffred, T. Heine, An atlas of two-dimensional materials. Chem. Soc. Rev. **43**, 6537–6554 (2014). https://doi.org/10.1039/c4cs00102h

40. M. Xu, T. Liang, M. Shi, H. Chen, Graphene-like two-dimensional materials. Chem. Rev. **113**, 3766–3798 (2013). https://doi.org/10.1021/cr300263a

41. C. Liu, H. Chen, S. Wang, Q. Liu, Y.-G. Jiang et al., Two-dimensional materials for next-generation computing technologies. Nat. Nanotechnol. **15**, 545–557 (2020). https://doi.org/10.1038/s41565-020-0724-3

42. A. VahidMohammadi, J. Rosen, Y. Gogotsi, The world of two-dimensional carbides and nitrides (MXenes). Science **372**, 1581 (2021). https://doi.org/10.1126/science.abf1581

43. J. Zhu, G. Xiao, X. Zuo, Two-dimensional black phosphorus: an emerging anode material for lithium-ion batteries. Nano-Micro Lett. **12**, 120 (2020). https://doi.org/10.1007/s40820-020-00453-x

44. R. Yang, Y. Fan, Y. Zhang, L. Mei, R. Zhu et al., 2D transition metal dichalcogenides for photocatalysis. Angew. Chem. Int. Ed. **62**, 2218016 (2023). https://doi.org/10.1002/anie.202218016

45. J. Cao, P. You, G. Tang, F. Yan, Two-dimensional materials for boosting the performance of perovskite solar cells: Fundamentals, materials and devices. Mater. Sci. Eng. R. Rep. **153**, 100727 (2023). https://doi.org/10.1016/j.mser.2023.100727

46. J.T. Wang, J.M. Ball, E.M. Barea, A. Abate, J.A. Alexander-Webber et al., Low-temperature processed electron collection layers of graphene/TiO$_2$ nanocomposites in thin film perovskite solar cells. Nano Lett. **14**, 724–730 (2014). https://doi.org/10.1021/nl403997a

47. O. Ergen, S. Gilbert, T. Pham, S. Turner, M. Tan et al., Graded bandgap perovskite solar cells. Nat. Mater. **16**, 522–525 (2017). https://doi.org/10.1038/nmat4795

48. N. Arora, M.I. Dar, A. Hinderhofer, N. Pellet, F. Schreiber et al., Perovskite solar cells with CuSCN hole extraction layers yield stabilized efficiencies greater than 20%. Science **358**, 768–771 (2017). https://doi.org/10.1126/science.aam5655

49. A. Agresti, A. Pazniak, S. Pescetelli, A. Di Vito, D. Rossi et al., Titanium-carbide MXenes for work function and interface engineering in perovskite solar cells. Nat. Mater. **18**, 1228–1234 (2019). https://doi.org/10.1038/s41563-019-0478-1

50. Y. Wang, T. Wu, J. Barbaud, W. Kong, D. Cui et al., Stabilizing heterostructures of soft perovskite semiconductors. Science **365**, 687–691 (2019). https://doi.org/10.1126/science.aax8018

51. Q. Zhou, J. Duan, X. Yang, Y. Duan, Q. Tang, Interfacial strain release from the WS$_2$/CsPbBr$_3$ van der waals heterostructure for 1.7 V voltage all-inorganic perovskite solar cells. Angew. Chem. Int. Ed. **59**, 21997–22001 (2020). https://doi.org/10.1002/anie.202010252

52. C. Zhang, S. Liang, W. Liu, F.T. Eickemeyer, X. Cai et al., Ti$_1$–graphene single-atom material for improved energy level alignment in perovskite solar cells. Nat. Energy **6**, 1154–1163 (2021). https://doi.org/10.1038/s41560-021-00944-0

53. S. Pescetelli, A. Agresti, G. Viskadouros, S. Razza, K. Rogdakis et al., Integration of two-dimensional materials-based perovskite solar panels into a stand-alone solar farm. Nat. Energy **7**, 597–607 (2022). https://doi.org/10.1038/s41560-022-01035-4

54. K.S. Novoselov, A. Mishchenko, A. Carvalho, A.H. Castro, Neto 2D materials and van der Waals heterostructures. Science **353**, eaac9439 (2016). https://doi.org/10.1126/science.aac9439

55. Y. Liu, Y. Huang, X. Duan, Van der Waals integration before and beyond two-dimensional materials. Nature **567**, 323–333 (2019). https://doi.org/10.1038/s41586-019-1013-x

56. S. Bellani, A. Bartolotta, A. Agresti, G. Calogero, G. Grancini et al., Solution-processed two-dimensional materials for next-generation photovoltaics. Chem. Soc. Rev. **50**, 11870–11965 (2021). https://doi.org/10.1039/d1cs00106j

57. B. Wang, J. Iocozzia, M. Zhang, M. Ye, S. Yan et al., The charge carrier dynamics, efficiency and stability of two-dimensional material-based perovskite solar cells. Chem. Soc. Rev. **48**, 4854–4891 (2019). https://doi.org/10.1039/c9cs00254e

58. T. Wang, F. Zheng, G. Tang, J. Cao, P. You et al., 2D WSe$_2$ flakes for synergistic modulation of grain growth and charge transfer in tin-based perovskite solar cells. Adv. Sci. **8**, e2004315 (2021). https://doi.org/10.1002/advs.202004315

59. T. Mahmoudi, Y. Wang, Y.-B. Hahn, Graphene and its derivatives for solar cells application. Nano Energy **47**, 51–65 (2018). https://doi.org/10.1016/j.nanoen.2018.02.047

60. X. Meng, J. Zhou, J. Hou, X. Tao, S.H. Cheung et al., Versatility of carbon enables all carbon based perovskite solar cells to achieve high efficiency and high stability. Adv. Mater. **30**, e1706975 (2018). https://doi.org/10.1002/adma.201706975

61. U.K. Aryal, M. Ahmadpour, V. Turkovic, H.-G. Rubahn, A. Di Carlo et al., 2D materials for organic and perovskite photovoltaics. Nano Energy **94**, 106833 (2022). https://doi.org/10.1016/j.nanoen.2021.106833

62. Z. Qin, Y. Chen, K. Zhu, Y. Zhao, Two-dimensional materials for perovskite solar cells with enhanced efficiency and stability. ACS Mater. Lett. **3**, 1402–1416 (2021). https://doi.org/10.1021/acsmaterialslett.1c00327

63. S. Chen, G. Shi, Two-dimensional materials for halide perovskite-based optoelectronic devices. Adv. Mater. **29**, 1605448 (2017). https://doi.org/10.1002/adma.201605448

64. A.K. Geim, I.V. Grigorieva, Van der waals heterostructures. Nature **499**, 419–425 (2013). https://doi.org/10.1038/nature12385

65. D. Akinwande, C. Huyghebaert, C.-H. Wang, M.I. Serna, S. Goossens et al., Graphene and two-dimensional materials for silicon technology. Nature **573**, 507–518 (2019). https://doi.org/10.1038/s41586-019-1573-9

66. C. Li, Q. Cao, F. Wang, Y. Xiao, Y. Li et al., Engineering graphene and TMDs based van der Waals heterostructures for photovoltaic and photoelectrochemical solar energy conversion. Chem. Soc. Rev. **47**, 4981–5037 (2018). https://doi.org/10.1039/c8cs00067k

67. F. Zhang, J. He, Y. Xiang, K. Zheng, B. Xue et al., Semi-metal-semiconductor transitions for monolayer antimonene nanosheets and their application in perovskite solar cells. Adv. Mater. **30**, e1803244 (2018). https://doi.org/10.1002/adma.201803244

68. N. Yang, F. Pei, J. Dou, Y. Zhao, Z. Huang et al., Improving heat transfer enables durable perovskite solar cells. Adv. Energy Mater. **12**, 2200869 (2022). https://doi.org/10.1002/aenm.202200869

69. L. Rao, X. Meng, S. Xiao, Z. Xing, Q. Fu et al., Wearable tin-based perovskite solar cells achieved by a crystallographic size effect. Angew. Chem. Int. Ed. **60**, 14693–14700 (2021). https://doi.org/10.1002/anie.202104201

70. S. Wu, Z. Li, M.-Q. Li, Y. Diao, F. Lin et al., 2D metal–organic framework for stable perovskite solar cells with minimized lead leakage. Nat. Nanotechnol. **15**, 934–940 (2020). https://doi.org/10.1038/s41565-020-0765-7

71. D. Zhao, D. Gao, X. Wu, B. Li, S. Zhang et al., Efficient and stable 3D/2D perovskite solar cells through vertical heterostructures with (BA)$_4$AgBiBr8 nanosheets. Adv. Mater. **34**, 2204661 (2022). https://doi.org/10.1002/adma.202204661

72. P. Hess, Fracture of perfect and defective graphene at the nanometer scale: is graphene the strongest material? J. Appl. Phys. **120**, 124303 (2016). https://doi.org/10.1063/1.4962542

73. C. Lee, X. Wei, J.W. Kysar, J. Hone, Measurement of the elastic properties and intrinsic strength of monolayer graphene. Science **321**, 385–388 (2008). https://doi.org/10.1126/science.1157996

74. Z. Niazi, A. Hagfeldt, E.K. Goharshadi, Recent progress on the use of graphene-based nanomaterials in perovskite solar cells. J. Mater. Chem. A **11**, 6659–6687 (2023). https://doi.org/10.1039/d2ta09985c

75. H. Kim, H.H. Kim, J.I. Jang, S.K. Lee, G.-W. Lee et al., Doping graphene with an atomically thin two dimensional molecular layer. Adv. Mater. **26**, 8141–8146 (2014). https://doi.org/10.1002/adma.201403196

76. S.V. Morozov, K.S. Novoselov, M.I. Katsnelson, F. Schedin, D.C. Elias et al., Giant intrinsic carrier mobilities in graphene and its bilayer. Phys. Rev. Lett. **100**, 016602 (2008). https://doi.org/10.1103/PhysRevLett.100.016602

77. J. Wu, H. Lin, D.J. Moss, K.P. Loh, B. Jia, Graphene oxide for photonics, electronics and optoelectronics. Nat. Rev. Chem. **7**, 162–183 (2023). https://doi.org/10.1038/s41570-022-00458-7

78. Z. Zhou, X. Li, M. Cai, F. Xie, Y. Wu et al., Stable inverted planar perovskite solar cells with low-temperature-processed hole-transport bilayer. Adv. Energy Mater. **7**, 1700763 (2017). https://doi.org/10.1002/aenm.201700763

79. S.-Y. Lee, S.-J. Park, Comprehensive review on synthesis and adsorption behaviors of graphene-based materials.

Carbon Lett. **13**, 73–87 (2012). https://doi.org/10.5714/cl.2012.13.2.073

80. M. Jin, H.-K. Jeong, W.J. Yu, D.J. Bae, B.R. Kang et al., Graphene oxide thin film field effect transistors without reduction. J. Phys. D Appl. Phys. **42**, 135109 (2009). https://doi.org/10.1088/0022-3727/42/13/135109

81. D. López-Díaz, J.A. Delgado-Notario, V. Clericò, E. Diez, M.D. Merchán et al., Towards understanding the Raman spectrum of graphene oxide: the effect of the chemical composition. Coatings **10**, 524 (2020). https://doi.org/10.3390/coatings10060524

82. Y. Shen, S. Yang, P. Zhou, Q. Sun, P. Wang et al., Evolution of the band-gap and optical properties of graphene oxide with controllable reduction level. Carbon **62**, 157–164 (2013). https://doi.org/10.1016/j.carbon.2013.06.007

83. K. Khan, A.K. Tareen, M. Aslam, R. Wang, Y. Zhang et al., Recent developments in emerging two-dimensional materials and their applications. J. Mater. Chem. C **8**, 387–440 (2020). https://doi.org/10.1039/c9tc04187g

84. Q. Fu, J. Han, X. Wang, P. Xu, T. Yao et al., Electrocatalysts: 2D transition metal dichalcogenides: design, modulation, and challenges in electrocatalysis. Adv. Mater. **33**, 2170045 (2021). https://doi.org/10.1002/ADMA.202170045

85. T. Liao, Z. Chen, Y. Kuang, Z. Ren, W. Yu et al., Small-size $Ti_3C_2T_x$ MXene nanosheets coated with metal-polyphenol nanodots for enhanced cancer photothermal therapy and anti-inflammation. Acta Biomater. **159**, 312–323 (2023). https://doi.org/10.1016/j.actbio.2023.01.049

86. J. Dai, X.C. Zeng, Bilayer phosphorene: effect of stacking order on bandgap and its potential applications in thin-film solar cells. J. Phys. Chem. Lett. **5**, 1289–1293 (2014). https://doi.org/10.1021/jz500409m

87. R. Roldán, A. Castellanos-Gomez, E. Cappelluti, F. Guinea, Strain engineering in semiconducting two-dimensional crystals. J. Phys. Condens. Matter **27**, 313201 (2015). https://doi.org/10.1088/0953-8984/27/31/313201

88. S. Zhang, W. Zhou, Y. Ma, J. Ji, B. Cai et al., Antimonene oxides: emerging tunable direct bandgap semiconductor and novel topological insulator. Nano Lett. **17**, 3434–3440 (2017). https://doi.org/10.1021/acs.nanolett.7b00297

89. W. Choi, N. Choudhary, G.H. Han, J. Park, D. Akinwande et al., Recent development of two-dimensional transition metal dichalcogenides and their applications. Mater. Today **20**, 116–130 (2017). https://doi.org/10.1016/j.mattod.2016.10.002

90. P. You, G. Tang, F. Yan, Two-dimensional materials in perovskite solar cells. Mater. Today Energy **11**, 128–158 (2019). https://doi.org/10.1016/j.mtener.2018.11.006

91. S. Aftab, M.Z. Iqbal, S. Hussain, H.H. Hegazy, M.A. Saeed, Transition metal dichalcogenides solar cells and integration with perovskites. Nano Energy **108**, 108249 (2023). https://doi.org/10.1016/j.nanoen.2023.108249

92. C. Martella, C. Mennucci, A. Lamperti, E. Cappelluti, F.B. de Mongeot et al., Designer shape anisotropy on transition-metal-dichalcogenide nanosheets. Adv. Mater. **30**, 1705615 (2018). https://doi.org/10.1002/adma.201705615

93. M.A. Saeed, A. Shahzad, K. Rasool, F. Mateen, J.-M. Oh et al., 2D MXene: a potential candidate for photovoltaic cells? A critical review. Adv. Sci. **9**, 2104743 (2022). https://doi.org/10.1002/advs.202104743

94. S. Palei, G. Murali, C.-H. Kim, I. In, S.-Y. Lee et al., A review on interface engineering of MXenes for perovskite solar cells. Nano-Micro Lett. **15**, 123 (2023). https://doi.org/10.1007/s40820-023-01083-9

95. S. Qamar, K. Fatima, N. Ullah, Z. Akhter, A. Waseem et al., Recent progress in use of MXene in perovskite solar cells: for interfacial modification, work-function tuning and additive engineering. Nanoscale **14**, 13018–13039 (2022). https://doi.org/10.1039/d2nr02799b

96. M. Naguib, M. Kurtoglu, V. Presser, J. Lu, J. Niu et al., Two-dimensional nanocrystals produced by exfoliation of Ti_3AlC_2. Adv. Mater. **23**, 4248–4253 (2011). https://doi.org/10.1002/adma.201102306

97. L. Yang, P. Li, J. Ma, X. Zhang, X.-F. Wang et al., MXenes for perovskite solar cells: progress and prospects. J. Energy Chem. **81**, 443–461 (2023). https://doi.org/10.1016/j.jechem.2023.02.041

98. L. Li, Y. Yu, G.J. Ye, Q. Ge, X. Ou et al., Black phosphorus field-effect transistors. Nat. Nanotechnol. **9**, 372–377 (2014). https://doi.org/10.1038/nnano.2014.35

99. S. Zhang, S. Guo, Z. Chen, Y. Wang, H. Gao et al., Recent progress in 2D group-VA semiconductors: from theory to experiment. Chem. Soc. Rev. **47**, 982–1021 (2018). https://doi.org/10.1039/c7cs00125h

100. Z. Wu, Y. Lyu, Y. Zhang, R. Ding, B. Zheng et al., Large-scale growth of few-layer two-dimensional black phosphorus. Nat. Mater. **20**, 1203–1209 (2021). https://doi.org/10.1038/s41563-021-01001-7

101. S. Zhang, Z. Yan, Y. Li, Z. Chen, H. Zeng, Atomically thin arsenene and antimonene: semimetal–semiconductor and indirect–direct band-gap transitions. Angew. Chem. Int. Ed. **54**, 3112–3115 (2015). https://doi.org/10.1002/anie.201411246

102. J. Qiao, X. Kong, Z.-X. Hu, F. Yang, W. Ji, High-mobility transport anisotropy and linear dichroism in few-layer black phosphorus. Nat. Commun. **5**, 4475 (2014). https://doi.org/10.1038/ncomms5475

103. L.F. Kourkoutis, J.H. Song, H.Y. Hwang, D.A. Muller, Microscopic origins for stabilizing room-temperature ferromagnetism in ultrathin manganite layers. Proc. Natl. Acad. Sci. U.S.A. **107**, 11682–11685 (2010). https://doi.org/10.1073/pnas.1005693107

104. C.R. Dean, A.F. Young, I. Meric, C. Lee, L. Wang et al., Boron nitride substrates for high-quality graphene electronics. Nat. Nanotechnol. **5**, 722–726 (2010). https://doi.org/10.1038/nnano.2010.172

105. C. Wang, Q. He, U. Halim, Y. Liu, E. Zhu et al., Monolayer atomic crystal molecular superlattices. Nature **555**, 231–236 (2018). https://doi.org/10.1038/nature25774

106. Y. Liu, J. Guo, E. Zhu, L. Liao, S.-J. Lee et al., Approaching the Schottky-Mott limit in van der Waals metal-semiconductor junctions. Nature **557**, 696–700 (2018). https://doi.org/10.1038/s41586-018-0129-8

107. Y. Liu, N.O. Weiss, X. Duan, H.-C. Cheng, Y. Huang et al., Van der Waals heterostructures and devices. Nat. Rev. Mater. **1**, 16042 (2016). https://doi.org/10.1038/natrevmats.2016.42

108. L. Liao, J. Bai, Y. Qu, Y.-C. Lin, Y. Li et al., High-κ oxide nanoribbons as gate dielectrics for high mobility top-gated graphene transistors. Proc. Natl. Acad. Sci. U.S.A. **107**, 6711–6715 (2010). https://doi.org/10.1073/pnas.0914117107

109. D. Jariwala, T.J. Marks, M.C. Hersam, Mixed-dimensional van der waals heterostructures. Nat. Mater. **16**, 170–181 (2017). https://doi.org/10.1038/nmat4703

110. Z. Wen, C. Liang, S. Li, G. Wang, B. He et al., High-quality van der waals epitaxial $CsPbBr_3$ film grownon monolayer graphene covered TiO_2 for high-performance solar cells. Energy Environ. Mater. **21**, 12680 (2023). https://doi.org/10.1002/eem2.12680

111. G. Tang, P. You, Q. Tai, A. Yang, J. Cao et al., Solution-phase epitaxial growth of perovskite films on 2D material flakes for high-performance solar cells. Adv. Mater. **31**, e1807689 (2019). https://doi.org/10.1002/adma.201807689

112. X. Yao, B. He, J. Zhu, J. Ti, L. Cui et al., Tailoring type-II all-in-one buried interface for 1635V-voltage, all-inorganic $CsPbBr_3$ perovskite solar cells. Nano Energy **96**, 107138 (2022). https://doi.org/10.1016/j.nanoen.2022.107138

113. Y. Han, T. Zuo, K. He, L. Yang, S. Zhan et al., 2D-Antimonene-assisted hetero-epitaxial growth of perovskite films for efficient solar cells. Mater. Today **61**, 54–64 (2022). https://doi.org/10.1016/j.mattod.2022.10.020

114. K.K. Paul, J.-H. Kim, Y.H. Lee, Hot carrier photovoltaics in van der Waals heterostructures. Nat. Rev. Phys. **3**, 178–192 (2021). https://doi.org/10.1038/s42254-020-00272-4

115. D.L. McGott, C.P. Muzzillo, C.L. Perkins, J.J. Berry, K. Zhu et al., 3D/2D passivation as a secret to success for polycrystalline thin-film solar cells. Joule **5**, 1057–1073 (2021). https://doi.org/10.1016/j.joule.2021.03.015

116. M. Zhu, C. Li, B. Li, J. Zhang, Y. Sun et al., Interaction engineering in organic–inorganic hybrid perovskite solar cells. Mater. Horiz. **7**, 2208–2236 (2020). https://doi.org/10.1039/d0mh00745e

117. T. Mahmoudi, Y. Wang, Y.-B. Hahn, Stability enhancement in perovskite solar cells with perovskite/silver–graphene composites in the active layer. ACS Energy Lett. **4**, 235–241 (2019). https://doi.org/10.1021/acsenergylett.8b02201

118. J. Cao, G. Tang, P. You, T. Wang, F. Zheng et al., Enhanced performance of planar perovskite solar cells induced by van der waals epitaxial growth of mixed perovskite films on WS_2 flakes. Adv. Funct. Mater. **30**, 2002358 (2020). https://doi.org/10.1002/adfm.202002358

119. F. Berry, R. Mermet-Lyaudoz, J.M. Cuevas Davila, D.A. Djemmah, H.S. Nguyen et al., Light management in perovskite photovoltaic solar cells: a perspective. Adv. Energy Mater. **12**, 2200505 (2022). https://doi.org/10.1002/aenm.202200505

120. C. Chen, S. Zheng, H. Song, Photon management to reduce energy loss in perovskite solar cells. Chem. Soc. Rev. **50**, 7250–7329 (2021). https://doi.org/10.1039/d0cs01488e

121. G. Yin, H. Zhao, J. Feng, J. Sun, J. Yan et al., Low-temperature and facile solution-processed two-dimensional TiS_2 as an effective electron transport layer for UV-stable planar perovskite solar cells. J. Mater. Chem. A **6**, 9132–9138 (2018). https://doi.org/10.1039/c8ta01143e

122. Z.-W. Gao, Y. Wang, H. Liu, J. Sun, J. Kim et al., Tailoring the interface in $FAPbI_3$ planar perovskite solar cells by imidazole-graphene-quantum-dots. Adv. Funct. Mater. **31**, 2101438 (2021). https://doi.org/10.1002/adfm.202101438

123. Q. Cai, W. Sheng, J. Yang, Y. Zhong, S. Xiao et al., Synergistic passivation and down-conversion by imidazole-modified graphene quantum dots for high performance and UV-resistant perovskite solar cells. Adv. Funct. Mater. **33**, 2304503 (2023). https://doi.org/10.1002/adfm.202304503

124. T. Guo, H. Wang, W. Han, J. Zhang, C. Wang et al., Designed p-type graphene quantum dots to heal interface charge transfer in Sn-Pb perovskite solar cells. Nano Energy **98**, 107298 (2022). https://doi.org/10.1016/j.nanoen.2022.107298

125. C. Wu, W. Fang, Q. Cheng, J. Wan, R. Wen et al., MXene-regulated perovskite vertical growth for high-performance solar cells. Angew. Chem. Int. Ed. **61**, 2210970 (2022). https://doi.org/10.1002/anie.202210970

126. R. Zhang, Z. Huang, W. Chen, B. Lyu, H. Zhang et al., A self-assembled vertical-gradient and well-dispersed MXene structure for flexible large-area perovskite modules. Adv. Funct. Mater. **33**, 2210063 (2023). https://doi.org/10.1002/adfm.202210063

127. J. He, G. Hu, Y. Jiang, S. Zeng, G. Niu et al., Dual-interface engineering in perovskite solar cells with 2D carbides. Angew. Chem. Int. Ed. **62**, e202311865 (2023). https://doi.org/10.1002/anie.202311865

128. J. Zhang, C. Huang, Y. Sun, H. Yu, Amino-functionalized niobium-carbide MXene serving as electron transport layer and perovskite additive for the preparation of high-performance and stable methylammonium-free perovskite solar cells. Adv. Funct. Mater. **32**, 2113367 (2022). https://doi.org/10.1002/adfm.202113367

129. M. Zhang, M. Ye, W. Wang, C. Ma, S. Wang et al., Synergistic cascade carrier extraction via dual interfacial positioning of ambipolar black phosphorene for high-efficiency perovskite solar cells. Adv. Mater. **32**, e2000999 (2020). https://doi.org/10.1002/adma.202000999

130. T.J. MacDonald, A.J. Clancy, W. Xu, Z. Jiang, C.-T. Lin et al., Phosphorene nanoribbon-augmented optoelectronics for enhanced hole extraction. J. Am. Chem. Soc. **143**, 21549–21559 (2021). https://doi.org/10.1021/jacs.1c08905

131. S.Y. Park, K. Zhu, Advances in SnO_2 for efficient and stable n-i-p perovskite solar cells. Adv. Mater. **34**, e2110438 (2022). https://doi.org/10.1002/adma.202110438

132. J. Um, S.E. Kim, *Homo*-junction pn diode using p-type SnO and n-type SnO_2 thin films. ECS Solid State Lett. **3**, P94–P98 (2014). https://doi.org/10.1149/2.0051408ssl

133. J.A. Hong, E.D. Jung, J.C. Yu, D.W. Kim, Y.S. Nam et al., Improved efficiency of perovskite solar cells using a nitrogen-doped graphene-oxide-treated tin oxide layer. ACS Appl. Mater. Interfaces **12**, 2417–2423 (2020). https://doi.org/10.1021/acsami.9b17705

134. J. Xie, K. Huang, X. Yu, Z. Yang, K. Xiao et al., Enhanced electronic properties of SnO_2 via electron transfer from graphene quantum dots for efficient perovskite solar cells. ACS Nano **11**, 9176–9182 (2017). https://doi.org/10.1021/acsnano.7b04070

135. Z. Zhu, J. Ma, Z. Wang, C. Mu, Z. Fan et al., Efficiency enhancement of perovskite solar cells through fast electron extraction: the role of graphene quantum dots. J. Am. Chem. Soc. **136**, 3760–3763 (2014). https://doi.org/10.1021/ja4132246

136. M.-L. Tsai, S.-H. Su, J.-K. Chang, D.-S. Tsai, C.-H. Chen et al., Monolayer MoS_2 heterojunction solar cells. ACS Nano **8**, 8317–8322 (2014). https://doi.org/10.1021/nn502776h

137. G. Kakavelakis, I. Paradisanos, B. Paci, A. Generosi, M. Papachatzakis et al., Extending the continuous operating lifetime of perovskite solar cells with a molybdenum disulfide hole extraction interlayer. Adv. Energy Mater. **8**, 1702287 (2018). https://doi.org/10.1002/aenm.201702287

138. D.-J. Xue, Y. Hou, S.-C. Liu, M. Wei, B. Chen et al., Regulating strain in perovskite thin films through charge-transport layers. Nat. Commun. **11**, 1514 (2020). https://doi.org/10.1038/s41467-020-15338-1

139. C. Zhu, X. Niu, Y. Fu, N. Li, C. Hu et al., Strain engineering in perovskite solar cells and its impacts on carrier dynamics. Nat. Commun. **10**, 815 (2019). https://doi.org/10.1038/s41467-019-08507-4

140. J. Zhao, Y. Deng, H. Wei, X. Zheng, Z. Yu et al., Strained hybrid perovskite thin films and their impact on the intrinsic stability of perovskite solar cells. Sci. Adv. **3**, 5616 (2017). https://doi.org/10.1126/sciadv.aao5616

141. J. Zhang, G. Hodes, Z. Jin, S.F. Liu, All-inorganic $CsPbX_3$ perovskite solar cells: progress and prospects. Angew. Chem. Int. Ed. **58**, 15596–15618 (2019). https://doi.org/10.1002/anie.201901081

142. Y. Rui, T. Li, B. Li, Y. Wang, P. Müller-Buschbaum, Two-dimensional SnS_2 nanosheets as electron transport and interfacial layers enable efficient perovskite solar cells. J. Mater. Chem. C **10**, 12392–12401 (2022). https://doi.org/10.1039/d2tc02452g

143. E. Zhao, L. Gao, S. Yang, L. Wang, J. Cao et al., *In situ* fabrication of 2D SnS_2 nanosheets as a new electron transport layer for perovskite solar cells. Nano Res. **11**, 5913–5923 (2018). https://doi.org/10.1007/s12274-018-2103-z

144. X. Zhao, S. Liu, H. Zhang, S.-Y. Chang, W. Huang et al., 20% efficient perovskite solar cells with 2D electron transporting layer. Adv. Funct. Mater. **29**, 1805168 (2019). https://doi.org/10.1002/adfm.201805168

145. Y. Yang, H. Lu, S. Feng, L. Yang, H. Dong et al., Modulation of perovskite crystallization processes towards highly efficient and stable perovskite solar cells with MXene quantum dot-modified SnO_2. Energy Environ. Sci. **14**, 3447–3454 (2021). https://doi.org/10.1039/D1EE00056J

146. M. Ghidiu, M.R. Lukatskaya, M.-Q. Zhao, Y. Gogotsi, M.W. Barsoum, Conductive two-dimensional titanium carbide 'clay' with high volumetric capacitance. Nature **516**, 78–81 (2014). https://doi.org/10.1038/nature13970

147. L. Yang, C. Dall'Agnese, Y. Dall'Agnese, Y. Gang Chen, Y.S. Gao, A.K. Jena, X.-F. Wang, Y. Gogotsi, T. Miyasaka, Surface-modified metallic $Ti_3C_2T_x$ MXene as electron transport layer for planar heterojunction perovskite solar cells, in *MXenes: from discovery to applications of two-dimensional metal carbides and nitrides*. ed. by Y. Gogotsi (Jenny Stanford Publishing, New York, 2023), pp.993–1011. https://doi.org/10.1201/9781003306511-50

148. B. Anasori, M.R. Lukatskaya, Y. Gogotsi, 2D metal carbides and nitrides (MXenes) for energy storage. Nat. Rev. Mater. **2**, 16098 (2017). https://doi.org/10.1038/natrevmats.2016.98

149. V. Kamysbayev, A.S. Filatov, H. Hu, X. Rui, F. Lagunas et al., Covalent surface modifications and superconductivity of two-dimensional metal carbide MXenes. Science **369**, 979–983 (2020). https://doi.org/10.1126/science.aba8311

150. J. Zhang, C. Huang, H. Yu, Modulate the work function of Nb_2CT_x MXene as the hole transport layer for perovskite solar cells. Appl. Phys. Lett. **119**, 033506 (2021). https://doi.org/10.1063/5.0057978

151. M. Zhu, Y. Osakada, S. Kim, M. Fujitsuka, T. Majima, Black phosphorus: a promising two dimensional visible and near-infrared-activated photocatalyst for hydrogen evolution. Appl. Catal. B Environ. **217**, 285–292 (2017). https://doi.org/10.1016/j.apcatb.2017.06.002x

152. H. Liu, Y. Du, Y. Deng, P.D. Ye, Semiconducting black phosphorus: synthesis, transport properties and electronic applications. Chem. Soc. Rev. **44**, 2732–2743 (2015). https://doi.org/10.1039/C4CS00257A

153. R.W. Keyes, The electrical properties of black phosphorus. Phys. Rev. **92**, 580–584 (1953). https://doi.org/10.1103/physrev.92.580

154. Y. Hou, C.O.R. Quiroz, S. Scheiner, W. Chen, T. Stubhan et al., Low-temperature and hysteresis-free electron-transporting layers for efficient, regular, and planar structure perovskite solar cells. Adv. Energy Mater. **5**, 1501056 (2015). https://doi.org/10.1002/aenm.201501056

155. N. Fu, C. Huang, P. Lin, M. Zhu, T. Li et al., Black phosphorus quantum dots as dual-functional electron-selective materials for efficient plastic perovskite solar cells. J. Mater. Chem. A **6**, 8886–8894 (2018). https://doi.org/10.1039/c8ta01408f

156. Y. Zhang, L. Xu, Y. Wu, Q. Zhou, Z. Shi et al., Double-layer synergistic optimization by functional black phosphorus quantum dots for high-efficiency and stable planar perovskite solar cells. Nano Energy **90**, 106610 (2021). https://doi.org/10.1016/j.nanoen.2021.106610

157. X. Wang, J. He, B. Zhou, Y. Zhang, J. Wu et al., Bandgap-tunable preparation of smooth and large two-dimensional antimonene. Angew. Chem. Int. Ed. **130**, 8804–8809 (2018). https://doi.org/10.1002/ange.201804886

158. N.H. Hemasiri, M. Ashraf, S. Kazim, R. Graf, R. Berger et al., Interface tweaking of perovskite solar cells with carbon nitride-based 2D materials. Nano Energy **109**, 108326 (2023). https://doi.org/10.1016/j.nanoen.2023.108326

159. J. Dou, C. Zhu, H. Wang, Y. Han, S. Ma et al., Synergistic effects of Eu-MOF on perovskite solar cells with improved stability. Adv. Mater. **33**, e2102947 (2021). https://doi.org/10.1002/adma.202102947

160. J. Lee, W.-C. Tian, W.-L. Wang, D.-X. Yao, Two-dimensional pnictogen honeycomb lattice: structure, on-site spin-orbit coupling and spin polarization. Sci. Rep. **5**, 11512 (2015). https://doi.org/10.1038/srep11512

161. S. Zhang, M. Xie, F. Li, Z. Yan, Y. Li et al., Semiconducting Group 15 monolayers: a broad range of band gaps and high carrier mobilities. Angew. Chem. Int. Ed. **128**, 1698–1701 (2016). https://doi.org/10.1002/ange.201507568

162. S. Sidhik, Y. Wang, M. De Siena, R. Asadpour, A.J. Torma et al., Deterministic fabrication of 3D/2D perovskite bilayer stacks for durable and efficient solar cells. Science **377**, 1425–1430 (2022). https://doi.org/10.1126/science.abq7652

163. G. Li, Y. Hu, M. Li, Y. Tang, Z. Zhang et al., Managing excess lead iodide with functionalized oxo-graphene nanosheets for stable perovskite solar cells. Angew. Chem. Int. Ed. **135**, 2307395 (2023). https://doi.org/10.1002/ange.202307395

164. S. Zhang, R. Guo, H. Zeng, Y. Zhao, X. Liu et al., Improved performance and stability of perovskite solar modules by interface modulating with graphene oxide crosslinked CsPbBr$_3$ quantum dots. Energy Environ. Sci. **15**, 244–253 (2022). https://doi.org/10.1039/d1ee01778k

165. N.H. Hemasiri, S. Kazim, S. Ahmad, Reduced trap density and mitigating the interfacial losses by placing 2D dichalcogenide material at perovskite/HTM interface in a dopant free perovskite solar cells. Nano Energy **77**, 105292 (2020). https://doi.org/10.1016/j.nanoen.2020.105292

166. H. Sui, B. He, J. Ti, S. Sun, W. Jiao et al., Sulfur vacancy defects healing of WS$_2$ quantum dots boosted hole extraction for all-inorganic perovskite solar cells. Chem. Eng. J. **455**, 140728 (2023). https://doi.org/10.1016/j.cej.2022.140728

167. M. Jin, C. Chen, F. Li, Z. Shen, H. Shen et al., Enhanced electrical properties in 2D perovskites via the bridging effect of SnS$_{1-x}$O$_2$x for perovskite solar cells with efficiency exceeding 24%. Nano Energy **109**, 108287 (2023). https://doi.org/10.1016/j.nanoen.2023.108287

168. T. Liu, Y. Liu, M. Chen, X. Guo, S. Tang et al., Fluorinated black phosphorene nanosheets with robust ambient stability for efficient and stable perovskite solar cells. Adv. Funct. Mater. **32**, 2106779 (2022). https://doi.org/10.1002/adfm.202106779

169. S. Liu, J. Lyu, D. Zhou, X. Zhuang, Z. Shi et al., Dual modification engineering via lanthanide-based halide quantum dots and black phosphorus enabled efficient perovskite solar cells with high open-voltage of 1235 V. Adv. Funct. Mater. **32**, 2112647 (2022). https://doi.org/10.1002/adfm.202112647

170. J.H. Heo, F. Zhang, J.K. Park, H. Joon Lee, D.S. Lee et al., Surface engineering with oxidized Ti$_3$C$_2$T$_x$ MXene enables efficient and stable p-i-n-structured CsPbI$_3$ perovskite solar cells. Joule **6**, 1672–1688 (2022). https://doi.org/10.1016/j.joule.2022.05.013

171. Y. Zhang, L. Xu, J. Sun, Y. Wu, Z. Kan et al., 24.11% high performance perovskite solar cells by dual interfacial carrier mobility enhancement and charge-carrier transport balance. Adv. Energy Mater. **12**, 2201269 (2022). https://doi.org/10.1002/aenm.202201269

172. C. Chen, J. Chen, H. Han, L. Chao, J. Hu et al., Perovskite solar cells based on screen-printed thin films. Nature **612**, 266–271 (2022). https://doi.org/10.1038/s41586-022-05346-0

173. G. Tong, J. Zhang, T. Bu, L.K. Ono, C. Zhang et al., Holistic strategies lead to enhanced efficiency and stability of hybrid chemical vapor deposition based perovskite solar cells and modules. Adv. Energy Mater. **13**, 2300153 (2023). https://doi.org/10.1002/aenm.202300153

174. Z. Liu, L. Qiu, L.K. Ono, S. He, Z. Hu et al., A holistic approach to interface stabilization for efficient perovskite solar modules with over 2,000-hour operational stability. Nat. Energy **5**, 596–604 (2020). https://doi.org/10.1038/s41560-020-0653-2

175. Q. Lou, G. Lou, H. Guo, T. Sun, C. Wang et al., Enhanced efficiency and stability of n-i-p perovskite solar cells by incorporation of fluorinated graphene in the spiro-OMeTAD hole transport layer. Adv. Energy Mater. **12**, 2201344 (2022). https://doi.org/10.1002/aenm.202201344

176. S.S. Bhosale, E. Jokar, A. Fathi, C.-M. Tsai, C.-Y. Wang et al., Functionalization of graphene oxide films with Au and MoO$_x$ nanoparticles as efficient *p*-contact electrodes for inverted planar perovskite solar cells. Adv. Funct. Mater. **28**, 1803200 (2018). https://doi.org/10.1002/adfm.201803200

177. J. Du, J. Duan, X. Yang, Y. Duan, Q. Zhou et al., P-type charge transfer doping of graphene oxide with (NiCo)$_{1-y}$Fe$_y$O$_x$ for air-stable, all-inorganic CsPbIBr$_2$ perovskite solar cells. Angew. Chem. Int. Ed. **60**, 10608–10613 (2021). https://doi.org/10.1002/anie.202016703

178. S.Y. Lee, U.J. Kim, J. Chung, H. Nam, H.Y. Jeong et al., Large work function modulation of monolayer MoS$_2$ by ambient gases. ACS Nano **10**, 6100–6107 (2016). https://doi.org/10.1021/acsnano.6b01742

179. T. Zhang, F. Wang, H. Kim, I. Choi, C. Wang, E. Cho et al., Ion-modulated radical doping of spiro-OMeTAD for more efficient and stable perovskite solar cells. Science **377**, 495–501 (2022). https://doi.org/10.1126/science.abo2757

180. J. Lee, T. Son, K. Min, S. Park, Y. Kim et al., Rationally designed hole transporting layer system for efficient and stable perovskite solar cells. EcoMat **5**, e12414 (2023). https://doi.org/10.1002/eom2.12414

181. X. Fan, N.E. Stott, J. Zeng, Y. Li, J. Ouyang et al., PEDOT:PSS materials for optoelectronics, thermoelectrics, and flexible and stretchable electronics. J. Mater. Chem. A **11**, 18561–18591 (2023). https://doi.org/10.1039/d3ta03213b

182. Q.H. Wang, K. Kalantar-Zadeh, A. Kis, J.N. Coleman, M.S. Strano, Electronics and optoelectronics of two-dimensional

transition metal dichalcogenides. Nat. Nanotechnol. **7**, 699–712 (2012). https://doi.org/10.1038/nnano.2012.193

183. L. Najafi, B. Taheri, B. Martín-García, S. Bellani, D. Di Girolamo et al., MoS_2 quantum dot/graphene hybrids for advanced interface engineering of a $CH_3NH_3PbI_3$ perovskite solar cell with an efficiency of over 20%. ACS Nano **12**, 10736–10754 (2018). https://doi.org/10.1021/acsnano.8b05514

184. A. Agresti, S. Pescetelli, A.L. Palma, B. Martín-García, L. Najafi et al., Two-dimensional material interface engineering for efficient perovskite large-area modules. ACS Energy Lett. **4**, 1862–1871 (2019). https://doi.org/10.1021/acsenergylett.9b01151

185. M. Karimipour, S. Khazraei, B.J. Kim, G. Boschloo, E.M.J. Johansson, Efficient and bending durable flexible perovskite solar cells via interface modification using a combination of thin MoS_2 nanosheets and molecules binding to the perovskite. Nano Energy **95**, 107044 (2022). https://doi.org/10.1016/j.nanoen.2022.107044

186. A. Di Vito, A. Pecchia, M. Auf der Maur, A. Di Carlo, Nonlinear work function tuning of lead-halide perovskites by MXenes with mixed terminations. Adv. Funct. Mater. **30**, 1909028 (2020). https://doi.org/10.1002/adfm.201909028

187. D. Saranin, S. Pescetelli, A. Pazniak, D. Rossi, A. Liedl et al., Transition metal carbides (MXenes) for efficient NiO-based inverted perovskite solar cells. Nano Energy **82**, 105771 (2021). https://doi.org/10.1016/j.nanoen.2021.105771

188. Q. Zhou, J. Duan, J. Du, Q. Guo, Q. Zhang et al., Tailored lattice "tape" to confine tensile interface for 11.08%-efficiency all-inorganic $CsPbBr_3$ perovskite solar cell with an ultrahigh voltage of 1.702 V. Adv. Sci. **8**, e2101418 (2021). https://doi.org/10.1002/advs.202101418

189. D. Xu, T. Li, Y. Han, X. He, S. Yang et al., Fluorine functionalized MXene QDs for near-record-efficiency $CsPbI_3$ solar cell with high open-circuit voltage. Adv. Funct. Mater. **32**, 2203704 (2022). https://doi.org/10.1002/adfm.202203704

190. P. Cai, L. Ding, Z. Chen, D. Wang, H. Peng et al., Tetrabutyl-ammonium bromide functionalized $Ti_3C_2T_x$ MXene as versatile cathode buffer layer for efficient and stable inverted perovskite solar cells. Adv. Funct. Mater. **33**, 2300113 (2023). https://doi.org/10.1002/adfm.202300113

191. P. Guo, C. Liu, X. Li, Z. Chen, H. Zhu et al., Laser manufactured nano-MXenes with tailored halogen terminations enable interfacial ionic stabilization of high performance perovskite solar cells. Adv. Energy Mater. **12**, 2202395 (2022). https://doi.org/10.1002/aenm.202202395

192. M. Karimipour, A. Paingott Parambil, K. Tabah Tanko, T. Zhang, F. Gao et al., Functionalized MXene/halide perovskite heterojunctions for perovskite solar cells stable under real outdoor conditions. Adv. Energy Mater. **13**, 2301959 (2023). https://doi.org/10.1002/aenm.202301959

193. B. Li, Y. Zhang, L. Fu, L. Zhang, Z. Liu et al., Two-dimensional black phosphorous induced exciton dissociation efficiency enhancement for high-performance all-inorganic $CsPbI_3$ perovskite photovoltaics. J. Mater. Chem. A **7**, 22539–22549 (2019). https://doi.org/10.1039/c9ta06016b

194. P. You, G. Tang, J. Cao, D. Shen, T.-W. Ng et al., 2D materials for conducting holes from grain boundaries in perovskite solar cells. Light Sci. Appl. **10**, 68 (2021). https://doi.org/10.1038/s41377-021-00515-8

195. J. He, F. Zhang, Y. Xiang, J. Lian, X. Wang et al., Preparation of low dimensional antimonene oxides and their application in cu: Nio_x based planar p-i-n perovskite solar cells. J. Power. Sources **435**, 226819 (2019). https://doi.org/10.1016/j.jpowsour.2019.226819

196. Z. Wang, Q. Lin, F.P. Chmiel, N. Sakai, L.M. Herz et al., Efficient ambient-air-stable solar cells with 2D–3D heterostructured butylammonium-caesium-formamidinium lead halide perovskites. Nat. Energy **2**, 17135 (2017). https://doi.org/10.1038/nenergy.2017.135

197. X. Liu, D. Luo, Z.-H. Lu, J.S. Yun, M. Saliba et al., Stabilization of photoactive phases for perovskite photovoltaics. Nat. Rev. Chem. **7**, 462–479 (2023). https://doi.org/10.1038/s41570-023-00492-z

198. C. Ma, F.T. Eickemeyer, S.-H. Lee, D.-H. Kang, S.J. Kwon et al., Unveiling facet-dependent degradation and facet engineering for stable perovskite solar cells. Science **379**, 173–178 (2023). https://doi.org/10.1126/science.adf3349

199. F. Zhang, S.Y. Park, C. Yao, H. Lu, S.P. Dunfield et al., Metastable *Dion*-Jacobson 2D structure enables efficient and stable perovskite solar cells. Science **375**, 71–76 (2022). https://doi.org/10.1126/science.abj2637

200. G. Grancini, M.K. Nazeeruddin, Dimensional tailoring of hybrid perovskites for photovoltaics. Nat. Rev. Mater. **4**, 4–22 (2019). https://doi.org/10.1038/s41578-018-0065-0

201. P. Chen, D. He, X. Huang, C. Zhang, L. Wang, Bilayer 2D–3D perovskite heterostructures for efficient and stable solar cells. ACS Nano **18**, 67–88 (2024). https://doi.org/10.1021/acsnano.3c09176

202. M. Shao, T. Bie, L. Yang, Y. Gao, X. Jin et al., Over 21% efficiency stable 2D perovskite solar cells. Adv. Mater. **34**, e2107211 (2022). https://doi.org/10.1002/adma.202107211

203. Y. Zhang, N.-G. Park, Quasi-two-dimensional perovskite solar cells with efficiency exceeding 22%. ACS Energy Lett. **7**, 757–765 (2022). https://doi.org/10.1021/acsenergylett.1c02645

204. R. Azmi, E. Ugur, A. Seitkhan, F. Aljamaan, A.S. Subbiah et al., Damp heat–stable perovskite solar cells with tailored-dimensionality 2D/3D heterojunctions. Science **376**, 73–77 (2022). https://doi.org/10.1126/science.abm5784

205. H. Chen, S. Teale, B. Chen, Y. Hou, L. Grater et al., Quantum-size-tuned heterostructures enable efficient and stable inverted perovskite solar cells. Nat. Photon. **16**, 352–358 (2022). https://doi.org/10.1038/s41566-022-00985-1

206. G. Yang, Z. Ren, K. Liu, M. Qin, W. Deng et al., Stable and low-photovoltage-loss perovskite solar cells by multifunctional passivation. Nat. Photon. **15**, 681–689 (2021). https://doi.org/10.1038/s41566-021-00829-4

207. B.-B. Yu, Z. Chen, Y. Zhu, Y. Wang, B. Han et al., Heterogeneous 2D/3D tin-halides perovskite solar cells with certified conversion efficiency breaking 14. Adv. Mater. **33**, e2102055 (2021). https://doi.org/10.1002/adma.202102055

208. Y.-W. Jang, S. Lee, K.M. Yeom, K. Jeong, K. Choi et al., Intact 2D/3D halide junction perovskite solar cells via solid-phase in-plane growth. Nat. Energy **6**, 63–71 (2021). https://doi.org/10.1038/s41560-020-00749-7

209. Z. Liu, P. You, C. Xie, G. Tang, F. Yan, Ultrathin and flexible perovskite solar cells with graphene transparent electrodes. Nano Energy **28**, 151–157 (2016). https://doi.org/10.1016/j.nanoen.2016.08.038

210. Y. Wu, G. Xu, J. Xi, Y. Shen, X. Wu et al., *In situ* crosslinking-assisted perovskite grain growth for mechanically robust flexible perovskite solar cells with 23.4% efficiency. Joule **7**, 398–415 (2023). https://doi.org/10.1016/j.joule.2022.12.013

211. Z. Chen, Q. Cheng, H. Chen, Y. Wu, J. Ding et al., Perovskite grain-boundary manipulation using room-temperature dynamic self-healing "ligaments" for developing highly stable flexible perovskite solar cells with 23.8% efficiency. Adv. Mater. **35**, 2300513 (2023). https://doi.org/10.1002/adma.202300513

212. Q. Luo, H. Ma, Q. Hou, Y. Li, J. Ren et al., All-carbon-electrode-based endurable flexible perovskite solar cells. Adv. Funct. Mater. **28**, 1706777 (2018). https://doi.org/10.1002/adfm.201706777

213. B.J. Kim, D.H. Kim, Y.-Y. Lee, H.-W. Shin, G.S. Han et al., Highly efficient and bending durable perovskite solar cells: toward a wearable power source. Energy Environ. Sci. **8**, 916–921 (2015). https://doi.org/10.1039/c4ee02441a

214. J.H. Heo, D.S. Lee, F. Zhang, C. Xiao, S.J. Heo et al., Super flexible transparent conducting oxide-free organic–inorganic hybrid perovskite solar cells with 19.01% efficiency (active area = 1 cm^2). Sol. RRL **5**, 2100733 (2021). https://doi.org/10.1002/solr.202100733

215. V.-D. Tran, S.V.N. Pammi, B.-J. Park, Y. Han, C. Jeon et al., Transfer-free graphene electrodes for super-flexible and semitransparent perovskite solar cells fabricated under ambient air. Nano Energy **65**, 104018 (2019). https://doi.org/10.1016/j.nanoen.2019.104018

216. J.H. Heo, D.H. Shin, M.H. Jang, M.L. Lee, M.G. Kang et al., Highly flexible, high-performance perovskite solar cells with adhesion promoted AuCl$_3$-doped graphene electrodes. J. Mater. Chem. A **5**, 21146–21152 (2017). https://doi.org/10.1039/c7ta06465a

217. J.H. Heo, D.H. Shin, D.H. Song, D.H. Kim, S.J. Lee et al., Super-flexible bis(trifluoromethanesulfonyl)-amide doped graphene transparent conductive electrodes for photo-stable perovskite solar cells. J. Mater. Chem. A **6**, 8251–8258 (2018). https://doi.org/10.1039/c8ta02672f

218. B.-J. Park, J.-S. Choi, H.-S. Kim, H.-Y. Kim, J.-R. Jeong et al., Realization of large-area wrinkle-free monolayer graphene films transferred to functional substrates. Sci. Rep. **5**, 9610 (2015). https://doi.org/10.1038/srep09610

219. X. Xu, H. Wang, J. Wang, M. Muhammad, Z. Wang et al., Surface functionalization of a graphene cathode to facilitate ALD growth of an electron transport layer and realize high-performance flexible perovskite solar cells. ACS Appl. Energy Mater. **3**, 4208–4216 (2020). https://doi.org/10.1021/acsaem.9b02191

220. C. Zhang, S. Wang, H. Zhang, Y. Feng, W. Tian et al., Efficient stable graphene-based perovskite solar cells with high flexibility in device assembling *via* modular architecture design. Energy Environ. Sci. **12**, 3585–3594 (2019). https://doi.org/10.1039/c9ee02391g

221. M. Tian, C.Y. Woo, J.W. Choi, J.-Y. Seo, J.-M. Kim et al., Printable free-standing hybrid graphene/dry-spun carbon nanotube films as multifunctional electrodes for highly stable perovskite solar cells. ACS Appl. Mater. Interfaces **12**, 54806–54814 (2020). https://doi.org/10.1021/acsami.0c17141

222. G. Jeong, D. Koo, J.-H. Woo, Y. Choi, E. Son et al., Highly efficient self-encapsulated flexible semitransparent perovskite solar cells via bifacial cation exchange. ACS Appl. Mater. Interfaces **14**, 33297–33305 (2022). https://doi.org/10.1021/acsami.2c08023

223. M.M. Tavakoli, M. Nasilowski, J. Zhao, M.G. Bawendi, J. Kong, Efficient semitransparent CsPbI$_3$ quantum dots photovoltaics using a graphene electrode. Small Meth. **3**, 1900449 (2019). https://doi.org/10.1002/smtd.201900449

224. Y. Zhu, S. Jia, J. Zheng, Y. Lin, Y. Wu et al., Facile synthesis of nitrogen-doped graphene frameworks for enhanced performance of hole transport material-free perovskite solar cells. J. Mater. Chem. C **6**, 3097–3103 (2018). https://doi.org/10.1039/C8TC00086G

225. M. Guo, C. Wei, C. Liu, K. Zhang, H. Su et al., Composite electrode based on single-atom Ni doped graphene for planar carbon-based perovskite solar cells. Mater. Des. **209**, 109972 (2021). https://doi.org/10.1016/J.MATDES.2021.109972

226. M. Ma, X. Zhang, X. Chen, H. Xiong, L. Xu et al., *In situ* imaging of the atomic phase transition dynamics in metal halide perovskites. Nat. Commun. **14**, 7142 (2023). https://doi.org/10.1038/s41467-023-42999-5

227. Y. Wang, Y. Wang, Recent progress in mxene layers materials for supercapacitors: High-performance electrodes. SmartMat **4**(1), e1130 (2022). https://doi.org/10.1002/smm2.1130

228. S.A. Hashemi, S. Ramakrishna, A.G. Aberle, Recent progress in flexible–wearable solar cells for self-powered electronic devices. Energy Environ. Sci. **13**, 685–743 (2020). https://doi.org/10.1039/c9ee03046h

229. K. Montazeri, M. Currie, L. Verger, P. Dianat, M.W. Barsoum et al., Beyond gold: spin-coated Ti$_3$C$_2$-based MXene photodetectors. Adv. Mater. **31**, 1903271 (2019). https://doi.org/10.1002/adma.201903271